© 2018. Published by The Company of Biologists Ltd | Development (2018) 145, dev155366. doi:10.1242/dev.155366

RESEARCH ARTICLE

Maternal Nanog is required for zebrafish embryo architecture and for cell viability during gastrulation

Marina Veil[1], Melanie Anna Schaechtle[1,2,*], Meijiang Gao[1,2,*], Viola Kirner[1], Lenka Buryanova[1], Rachel Grethen[1] and Daria Onichtchouk[1,2,3,‡]

ABSTRACT

Nanog has been implicated in establishment of pluripotency in mammals and in zygotic genome activation in zebrafish. In this study, we characterize the development of MZ*nanog* (maternal and zygotic null) mutant zebrafish embryos. Without functional Nanog, epiboly is severely affected, embryo axes do not form and massive cell death starts at the end of gastrulation. We show that three independent defects in MZ*nanog* mutants contribute to epiboly failure: yolk microtubule organization required for epiboly is abnormal, maternal mRNA fails to degrade owing to the absence of miR-430, and actin structure of the yolk syncytial layer does not form properly. We further demonstrate that the cell death in MZ*nanog* embryos is cell-autonomous. Nanog is necessary for correct spatial expression of the ventral-specifying genes *bmp2b*, *vox* and *vent*, and the neural transcription factor *her3*. It is also required for the correctly timed activation of endoderm genes and for the degradation of maternal *eomesa* mRNA via miR-430. Our findings suggest that maternal Nanog coordinates several gene regulatory networks that shape the embryo during gastrulation.

KEY WORDS: Nanog, ZGA, Epiboly, Mutant, Transcription factor, Zebrafish

INTRODUCTION

The transcription factors Oct4 (known as Pou5f1 in mammals and Pou5f3 in zebrafish), Sox2 and Nanog are best known for their prominent functions as regulators of pluripotency in embryonic stem cells (ESCs) (Mitsui et al., 2003; Boyer et al., 2005; Loh et al., 2006), and their ability to reprogram somatic cells to a pluripotent state (Takahashi and Yamanaka, 2006; Silva et al., 2009). In developing embryos, Oct4 and Nanog also play distinct roles during the transition from cell pluripotency to terminal differentiation (Teo et al., 2011; Loh and Lim, 2011; Thomson et al., 2011; Frum et al., 2013; Radzisheuskaya et al., 2013; Le Bin et al., 2014). The question of how the same transcription factors can regulate seemingly opposing processes, such as pluripotency maintenance and cell differentiation, is far from being resolved. Functional studies on zebrafish and *Xenopus*, in which the earliest developmental stages are experimentally tractable, have large potential to contribute to our understanding of this question. Zebrafish Nanog, which is the functional ortholog to mouse Nanog in cross-species rescue assays, enables efficient reprogramming of mammalian *Nanog*$^{-/-}$ somatic cells to full pluripotency (Theunissen et al., 2011). Integration of Nanog into the embryonic early zygotic gene network will be useful to decode how pluripotency, patterning, and cell differentiation are coupled in the vertebrate embryo.

Zebrafish Nanog is abundantly translated during the transcriptionally silent period preceding zygotic genome activation (ZGA; Lee et al., 2013). At zebrafish ZGA, the first major wave of zygotic transcription occurs and a large specific subset of maternal transcripts is cleared by the microRNA miR-430 (Giraldez et al., 2006). Maternal Nanog has been implicated in both processes. Nanog regulates the post-ZGA clearance by directly activating miR-430 (Lee et al., 2013). Together with Pou5f3 and the SoxB1 family, maternal Nanog acts to activate transcription during ZGA. The combined loss of these factors results in the failure of the activation of >75% of zygotically transcribed genes (Lee et al., 2013; Leichsenring et al., 2013). Single loss-of-function phenotypes for SoxB1 group genes (Okuda et al., 2010), Oct4/Pou5f3 (Reim et al., 2004; Lunde et al., 2004) and Nanog differ significantly, suggesting overlapping as well as separate functions in the embryo during gastrulation stages (Onichtchouk and Driever, 2016).

The zebrafish epiboly movement involves the thinning and spreading of a multilayered sheet of cells over the yolk (Solnica-Krezel, 2006; Bruce, 2016). The zebrafish blastula embryo consists of the deep embryonic cells of the blastoderm and three extra-embryonic structures: a large yolk cell surrounded by a microtubule-rich cortical layer (yolk cytoplasmic layer or YCL), the underlying deep cells of the yolk syncytial layer (YSL), and the enveloping layer (EVL). Epiboly initiation commences with doming when the yolk cell bulges upward into the blastoderm (Kimmel et al., 1995), accompanied by the radial intercalation of the deep cells (Warga and Kimmel, 1990). Two different types of cytoskeletal structures forming in the extra-embryonic layers are crucial for epiboly: microtubules of the YCL (Solnica-Krezel and Driever, 1994) and microfilaments of the YSL. The second phase of epiboly depends on deep cell motility and on the F-actin microfilament ring which forms at the border of the YSL and the EVL (Zalik et al., 1999; Cheng et al., 2004; Koppen et al., 2006).

Previous studies indicate that three transcription factors are involved in epiboly control: Pou5f3, Eomesodermin a (*eomesa*) and Mxtx2. In the maternal-zygotic (MZ) mutant of Pou5f3, MZ*spg* (*Spiel-ohne-Grenzen*), two crucial components driving epiboly are severely affected: microtubules of the YCL and radial intercalation of deep cells (Reim and Brand, 2006; Lachnit et al., 2008; Song et al., 2013). Oct4/Pou5f3 mutants also show multiple independent patterning defects (Reim et al., 2004; Lunde et al., 2004; Belting et al., 2011), and increased apoptosis at the end of gastrulation (Kotkamp et al., 2014). In contrast, only epiboly movements are

[1]Developmental Biology, Institute Biology I, Faculty of Biology, Albert Ludwigs University of Freiburg, 79104 Freiburg, Germany. [2]BIOSS Centre for Biological Signalling Studies, Albert Ludwigs University of Freiburg, 79104 Freiburg, Germany. [3]Institute of Developmental Biology RAS, 119991 Moscow, Russia.
*These authors contributed equally to this work

‡Author for correspondence (daria.onichtchouk@biologie.uni-freiburg.de)

V.K., 0000-0001-5845-1267; L.B., 0000-0002-9341-0951; R.G., 0000-0002-7404-7771; D.O., 0000-0001-6497-1445

Received 26 May 2017; Accepted 7 November 2017

Development (2018) 145, dev155366. doi:10.1242/dev.155366

critically affected in MZ*eomesa* mutants and in Mxtx2 knockdown (KD) embryos. MZ*eomesa* mutants show a delay in doming and YCL microtubule defects. However, once started, epiboly progresses normally (Du et al., 2012). Mxtx2 is expressed shortly after ZGA and is specifically required for epiboly within the YSL. In Mxtx2 KD embryos, epiboly initiation occurs normally and YCL microtubules are not affected, but epiboly progression is impaired owing to abnormal F-actin ring formation and reduced motility of deep cells (Hirata et al., 2000; Bruce et al., 2005; Wilkins et al., 2008).

A zebrafish Nanog morpholino KD phenotype was previously described in two studies (Schuff et al., 2011; Xu et al., 2012). The main features of the KD phenotype are abnormal morphogenetic movements and embryo death at the end of gastrulation. Xu et al. (2012) demonstrated that in Nanog KD embryos expression of *mxtx2* and Nodal pathway genes in the YSL is absent. Epiboly and the normal expression of Nodal pathway genes could be rescued by injection of *mxtx2* mRNA into the Nanog KD embryos. These experiments led to the two-step model of action of Nanog via the YSL: Nanog activates *mxtx2* in the YSL and Mxtx2 induces the expression of the ligands of Nodal family genes, which send their signals to the embryonic cells.

Poor correlation between morpholino-induced and mutant phenotypes, as observed on a large scale in zebrafish, led to the suggestion that mutant phenotypes should become the standard metric to define gene function in zebrafish (Kok et al., 2015). Thus, to understand the functions of Nanog, complete and reproducible genetic ablation of its gene activity was necessary. Here, we used transcription activator-like effector nucleases (TALENs) to create new mutant alleles to investigate the requirements of Nanog in zebrafish development. We show that both initiation (yolk doming), as well as progression of epiboly is impaired in MZ*nanog* embryos. Embryonic axial structures do not form and massive cell death starts at the end of gastrulation. Our data and published literature indicate that Nanog regulates three independent events that contribute to normal epiboly progression. These are: (1) spatial arrangement of microtubule structures in the yolk cortex, (2) Mxtx2-dependent gene expression in the YSL, and (3) miR-430-dependent degradation of maternal mRNAs in deep embryonic cells. Furthermore, Nanog regulates cell survival. This function can be distinguished from the function Nanog serves during epiboly. Using transplantation experiments, we demonstrate that the survival of early blastula-stage MZ*nanog*$^{-/-}$ cells is reduced even in the wild-type embryo environment. We observe multiple changes in expression timing and patterns of known developmental regulators. This is compatible with the global role of Nanog in zygotic genome activation.

RESULTS

MZ*nanog* embryos arrest in gastrulation and show a delay in epiboly movements

We introduced a mutation into the first exon of the *nanog* gene to analyze the function of zebrafish Nanog using the TALEN technique (Cermak et al., 2011). This resulted in a deletion of 10 bp and a frame shift after amino acid 17 with a stop codon after 15 additional amino acids (Fig. 1A). Whereas the zygotic homozygous mutants were viable and fertile, the maternal (M) and maternal-zygotic (MZ) mutants showed severe developmental defects (Fig. 1B, Movie 1). After blastula stage [4 hours post-fertilization (hpf)], MZ*nanog* and M*nanog* embryos were delayed in their epiboly movements and a shield-like structure appeared later than in wild-type controls (Fig. 1B, 4-8 hpf). At 8 hpf, epiboly movements were partially restored in M*nanog*, whereas MZ*nanog* embryos formed an enlarged shield and underwent developmental arrest (Fig. 1B, 8 hpf). This was often followed by yolk lysis and detachment of blastoderm from the yolk (Fig. 1C, Movie 1). MZ*nanog* embryos that survived until 24 hpf consisted of unstructured cell masses with no recognizable body axis. In M*nanog* mutant embryos, a short body axis of anterior type was often present (Fig. 1B, 24 hpf). MZ*nanog* mutants could be rescued by injecting *nanog* mRNA into 1-cell-stage embryos, resulting in fertile adults (see Fig. 5).

Cell death at the end of gastrulation is increased in Nanog mutants

Nanog mRNA and protein are present in the germline of the ovary and testes (Wang et al., 2016). Therefore, Nanog might be required during oogenesis and the earliest developmental stages. We tested whether pre-ZGA cleavages occur normally in MZ*nanog* mutants by comparing three parallel time-lapse recordings of the wild-type and MZ*nanog* embryos (Movie 1). We did not detect any significant differences in cell cleavage rates before ZGA by live observations (Fig. S1A), or in cell division rates at blastula stages by scoring mitotic cells (Fig. S1B-D, Table S1, Materials and Methods). We next addressed whether cell survival is affected in the MZ and M*nanog* mutants in respect to the wild type. Using Acridine Orange staining of living embryos (Materials and Methods, Fig. S2), we detected massive cell death in MZ*nanog* mutants after 10 hpf (Fig. 2A). The amount of dead cells in M*nanog* mutants was reduced compared with MZ*nanog* (Fig. 2B), but exceeded the that of wild-type controls (Fig. 2C,D; $P<10^{-6}$, Student's *t*-test).

MZ*nanog* embryos do not express *mxtx2* and have reduced and delayed expression of Nodal endodermal targets

We performed *in situ* hybridization to compare the expression of zygotic YSL genes and mesendodermal markers as well as maternal *eomesa* mRNA between wild-type and MZ*nanog* embryos. *mxtx2* transcripts were not detectable in MZ*nanog* and M*nanog* at any stage examined (Fig. 3A). Expression of the early endoderm-specifying genes *sox32* (Alexander et al., 1999), *mixer* (*mixl1*) (Henry and Melton, 1998) and *gata5* (Reiter et al., 1999) started later and was reduced compared with wild-type embryos. This reduction was not due to a general ZGA delay: the zygotic mesoderm markers *ntl* (*ta*) and *foxd3* (Schulte-Merker et al., 1994; Chen and Kimelman, 2000; Dougan et al., 2003) started at the appropriate time and were distributed similarly to the wild type in blastula (Fig. 3B,C, Fig. S3). At later stages, *ntl* was slightly reduced in MZ*nanog* compared with wild type (Fig. 3F). Maternal *eomesa* mRNA (Du et al., 2012) was abundant in both genotypes at 4 hpf and remained in 6 hpf MZ*nanog* whereas it was cleared from the wild type (Fig. 3B,G). We analyzed the expression of the definitive endodermal marker *sox17* (Alexander and Stainier, 1999) to address whether Nodal signaling is active and whether endoderm forms in M*nanog* and MZ*nanog*. Variously shaped marginal domains of *sox32* and *sox17* expression were detectable in MZ*nanog* mutants at 8 hpf. MZ*spg* mutants, which lack *sox17* expression (Lunde et al., 2004; Reim et al., 2004), were stained in parallel and are shown for comparison (Fig. 3D). *Sox17*-positive endodermal cells were distinguishable in MZ*nanog* and M*nanog* mutants at 9 hpf, although their numbers were smaller compared with wild-type embryos (Fig. 3E, arrows). We concluded that Nodal signaling is reduced but not absent in MZ*nanog* embryos.

Both actin and tubulin cytoskeletal yolk structures of the yolk cell are abnormal in MZ*nanog*

Morphological defects in Nanog-like morphants have been explained by the abnormal extra-embryonic YSL structure (Xu

Development (2018) 145, dev155366. doi:10.1242/dev.155366

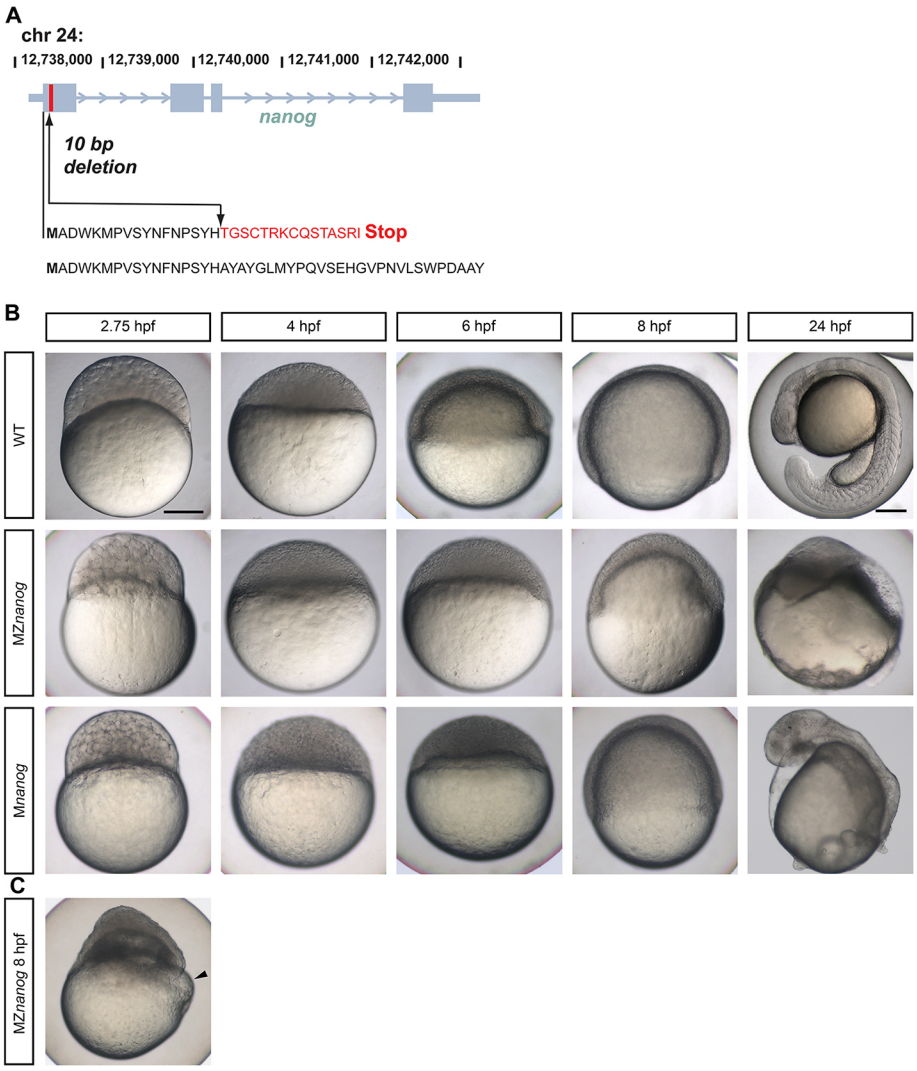

Fig. 1. Live phenotypes of Nanog mutants. (A) Scheme of the introduced mutation in the zebrafish *nanog* gene by TALENs. In the first exon 10 bp were deleted (arrow). Amino acids changed in the *nanog* mutant are shown in red. The wild-type Nanog amino acid sequence is shown beneath. (B) Lateral view of wild-type (WT), MZ*nanog* and M*nanog* embryos from 2.75 to 24 hpf. (C) Blastoderm detachment and start of yolk lysis (arrowhead) in an MZ*nanog* embryo. Scale bar: 200 µm.

et al., 2012), which prompted us to examine MZ*nanog* embryos for the presence of YSL and its morphology. We compared initial YSL formation in MZ*nanog* and the wild type and found that it was not distinguishable from the controls until sphere stage (Fig. 4A-D). At sphere stage, nuclei within the YSL undergo three rapid divisions and become post-mitotic. As epiboly begins, nuclei align at the periphery to form one row and some nuclei move from the periphery to the center underneath the blastoderm (Kimmel and Law, 1985; Kane et al., 1992; D'Amico and Cooper, 2001). To visualize these movements, we labeled the YSL nuclei by injecting the SYTOX Green vital dye and performed time-lapse recordings of the living embryos (Movie 2 for wild type and Movie 3 for MZ*nanog*, Fig. 4E-L). Although no differences could be detected between genotypes in number or positioning of nuclei at blastula stages (Fig. 4E-H′), in MZ*nanog* the nuclei did not align at the periphery of the YSL (compare Fig. 4I and 4J), centripetal migration of the YSL nuclei did not occur (Fig. 4K,L, boxed areas), and the doming of the yolk did not start (Fig. 4K′,L′, yellow arrows). The

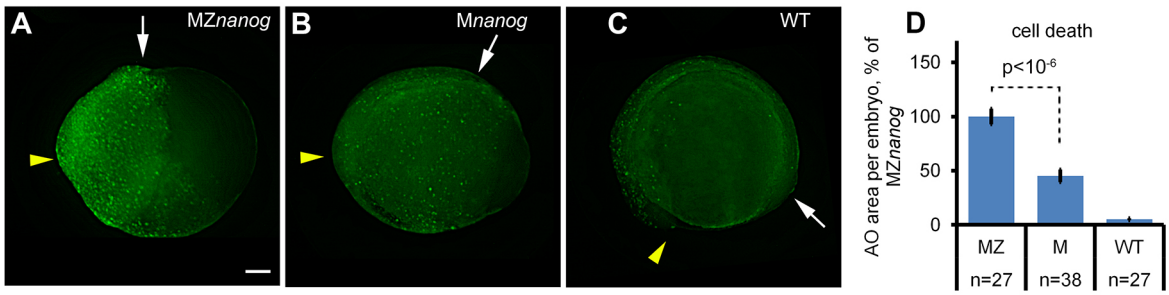

Fig. 2. Cell death is increased in Nanog mutants. (A-C) Groups of Acridine Orange (AO)-stained dead cells in 12 hpf MZ*nanog* (A), M*nanog* (B) and wild-type (WT, C) embryos are visible as green spots. Yellow arrowheads and white arrows point to anterior and posterior ends of dorsal embryo axes, respectively. Scale bar: 100 µm. (D) The increase in cell death in MZ*nanog* over M*nanog* is statistically significant ($P<10^{-6}$, Student's *t*-test); *n*, number of scored embryos. Error bars represent s.e.m.

Development (2018) 145, dev155366. doi:10.1242/dev.155366

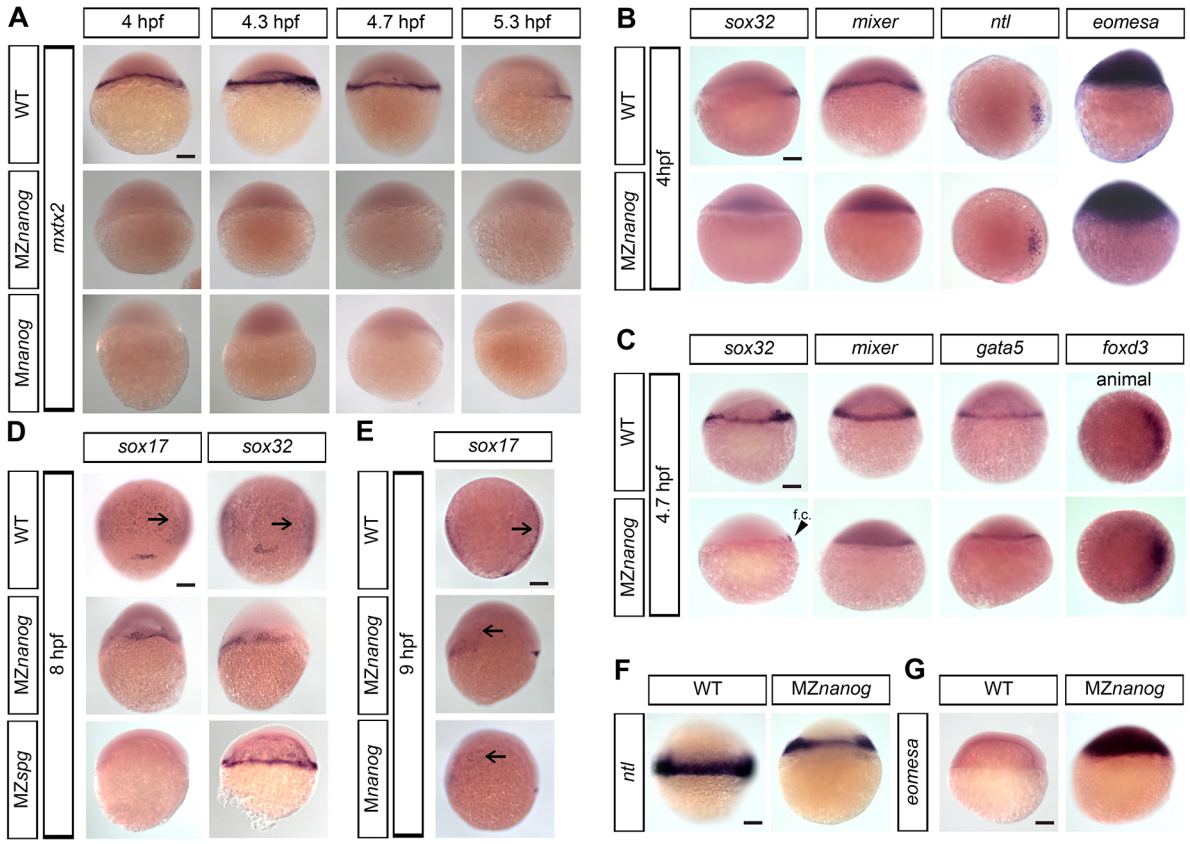

Fig. 3. Expression of *mxtx2*, *eomesa* and endomesodermal markers in Nanog mutants. Expression of the indicated genes in wild-type (WT), M*nanog* and MZ*nanog* embryos was visualized by *in situ* hybridization. Dorsal is to the right. (A) *mxtx2* expression is absent in MZ*nanog* and M*nanog* (lateral view). (B) Sphere stage expression of *sox32*, *mixer* and *eomesa* (lateral view) and *ntl* (animal view). Note that *sox32* and *mixer* are not detectable in MZ*nanog*, but *ntl* and *eomesa* expression is not altered. (C) 30% epiboly stage expression for *sox32*, *mixer*, *gata5* (lateral view) and *foxD3* (animal view). *f.c., forerunner cells* (arrowhead). (D) *sox17* and *sox32* staining at 8 hpf in WT, MZ*nanog* and MZ*spg* (dorsal view). Note that *sox17* and *sox32* are *both* expressed in MZ*nanog*, but only *sox32* is expressed in MZ*spg*. (E) *sox17* staining *in* WT, MZ*nanog* and M*nanog* (9 hpf, lateral view). In D,E, arrows show scattered endodermal cells. (F) *ntl* expression at 6 hpf (lateral view). (G) *eomesa* expression at 5.3 hpf (lateral view). Scale bars: 100 µm.

absence of yolk doming in MZ*nanog* was confirmed using light-sheet microscopy (Fig. 4M,N). To test whether the F-actin ring is impaired in MZ*nanog*, we visualized microfilament structures in wild type and MZ*nanog* using rhodamine-phalloidin staining. The F-actin ring with a row of endocytic vesicles was readily detectable in the wild type, but was strongly reduced in MZ*nanog* embryos (Fig. 4O-P′, Fig. S4). We next compared yolk cortical microtubules between wild type, MZ*nanog* and MZ*spg* mutants, in which abnormalities of YCL microtubule structure were previously reported (Lachnit et al., 2008) (Fig. 4Q-S′). As can be seen from Fig. 4R,R′, the yolk cell of MZ*nanog* formed a severely altered array of cortical microtubules resembling the MZ*spg* YCL phenotype (Fig. 4S,S′), but with more irregular with asymmetric holes between microtubule bundles. The large patches of microtubule-free areas in MZ*nanog* could be a reason for the yolk lysis observed at gastrulation (compare Fig. 1C and Fig. 4R). Thus, Nanog mutation affects the cytoskeletal architecture of two extra-embryonic yolk structures: microfilaments in the YSL and cortical microtubule arrays in the YCL.

All aspects of the MZ*nanog* mutant phenotype can be rescued by *nanog* mRNA

We performed a set of rescue experiments to test whether MZ*nanog* mutant defects can be restored by microinjections of *nanog* mRNA either in the YSL or in the whole embryo at the 1-cell stage (Fig. 5). Injection of *nanog* mRNA into MZ*nanog* embryos at the 1-cell stage resulted in restoration of epiboly and complete body axis (Fig. 5B,F,J, P) and rescue of the cell death (Fig. 5Q,R). The rescued embryos could be grown to fertile adults. After *nanog* mRNA was injected into the YSL, some MZ*nanog* embryos displayed a transient improvement in epiboly, but they could neither complete epiboly nor form a body axis (Fig. 5D,H,L,P). The lack of rescue by *nanog* mRNA injection into the YSL could be explained by insufficient time for translation of injected *nanog* mRNA. Indeed, injection of *nanog* mRNA into MZ*nanog* embryos restored *mxtx2* expression when *nanog* mRNA was injected at the 1-cell stage (Fig. 6F) but not when it was injected into the YSL (data not shown).

Mxtx2 and miR-430 injections rescue epiboly in MZ*nanog* mutants using different molecular mechanisms

Zygotic *mxtx2* mRNA is expressed in wild-type embryos after ZGA (Hirata et al., 2000) and, in that case, microinjection of mRNA at the 512-cell stage should suffice to restore the function of Mxtx2 in the YSL of MZ*nanog* embryos. To address whether some or all aspects of the MZ*nanog* phenotype can be rescued by Mxtx2, we injected a range of *mxtx2* mRNA concentrations into 1-cell stage or into the YSL of MZ*nanog* embryos (Fig. S5). Surprisingly, microinjection of *mxtx2* mRNA in the YSL did not rescue epiboly, but 1-cell-stage injection in MZ*nanog* resulted in complete epiboly rescue (Fig. 6A, Fig. S5).

Development (2018) 145, dev155366. doi:10.1242/dev.155366

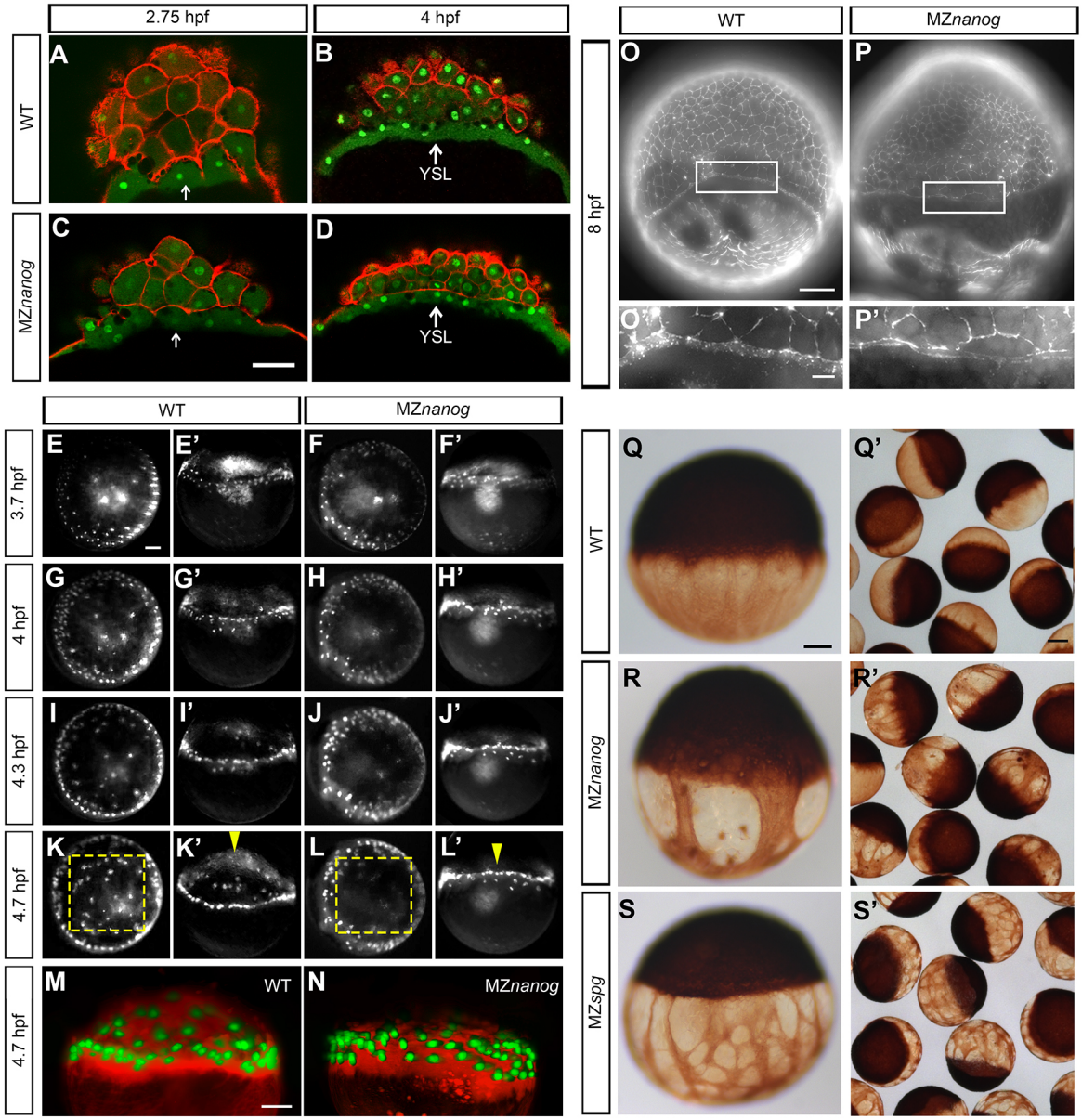

Fig. 4. Multiple abnormalities in MZ*nanog* embryo architecture. (A-D) YSL (white arrows) forms normally in MZ*nanog*. Lateral optical sections of wild type (WT; A,B) and MZ*nanog* (C,D) stained for nuclei (SYTOX green) and cell membranes (rhodamine-phalloidin) at the 512-cell (A,C) and sphere (B,D) stages. (E-L′) Animal (E-L) and lateral (E′-L′) view of SYTOX Green-injected WT and MZ*nanog* embryos in images captured from time-lapse recording (Movies 2 and 3). (E-H′) At oblong (E-F′) and sphere (G-H′) stages YSL nuclei of WT and MZ*nanog* show no difference; two to three rows of YSL nuclei are visible in the periphery of blastoderm. (I-J′) Early dome stage (before the doming starts). (I,I′) In a WT embryo, YSL nuclei are compacted and aligned in one row in the periphery of blastoderm. (J,J′) In MZ*nanog*, YSL nuclei do not compact; nuclei distribution is similar to sphere stage. (K-L′) 30% epiboly. In the WT (K,K′), but not in MZ*nanog* (L,L′), some YSL nuclei move from periphery to the central region and doming occurs (compare yellow boxes that frame the YSL centers in K and L and yellow arrowheads that point to the YSL center in K′ and L′). (M,N) Yolk doming is visible in WT (M), but not MZ*nanog* (N) at 4.7 hpf. Lateral view. YSL and YSL nuclei were labeled by tetramethylrhodamine-dextran and SYTOX Green co-injection. (O-P′) Actin was stained with rhodamine phalloidin in WT (O) and MZ*nanog* (P) embryos, 8 hpf. O′ and P′ are magnifications of the boxed areas showing the EVL-YSL border. The punctate F-actin ring colocalized with vesicles is visible in the EVL-YSL border in the WT; no vesicles and two tiny rings are visible in MZ*nanog*. (Q-S′) YCL microtubules were visualized by anti-tubulin staining at 6 hpf in WT (Q,Q′), MZ*nanog* (R,R′) and MZ*spg* (S,S′) embryos. Scale bars: 100 µm (A-D,E-L',M-P,Q-S); 20 µm (O′,P′); 200 µm (Q′,R′,S′).

Severe epiboly delay was seen in the MZ*dicer* mutants, in which the whole RNA degradation pathway is inactive (Giraldez et al., 2005). Therefore, it is possible that aberrant accumulation of maternal miR-430 targets contributes to epiboly defects in MZ*nanog*. We further tested, using the same experimental set-up as above, whether miR-430 contributes to any of the aspects of MZ*nanog* phenotype. Indeed, 1-cell-stage but not YSL microinjection of miR-430 rescued epiboly (Fig. 6A, Fig. S6).

We next investigated whether the cell death phenotype of MZ*nanog* could be rescued by *mxtx2* or miR-430. We found that neither injection reduced the number of dying cells in MZ*nanog* embryos (Fig. 6B,D). Formation of embryonic axes of variable length was often observed in *mxtx2*-injected MZ*nanog* embryos (Fig. 6C, Fig. S5); however, overall survival and axis formation rates varied from experiment to experiment. When directly compared with *nanog* mRNA-injected embryos of the same MZ*nanog* experimental batch,

Development (2018) 145, dev155366. doi:10.1242/dev.155366

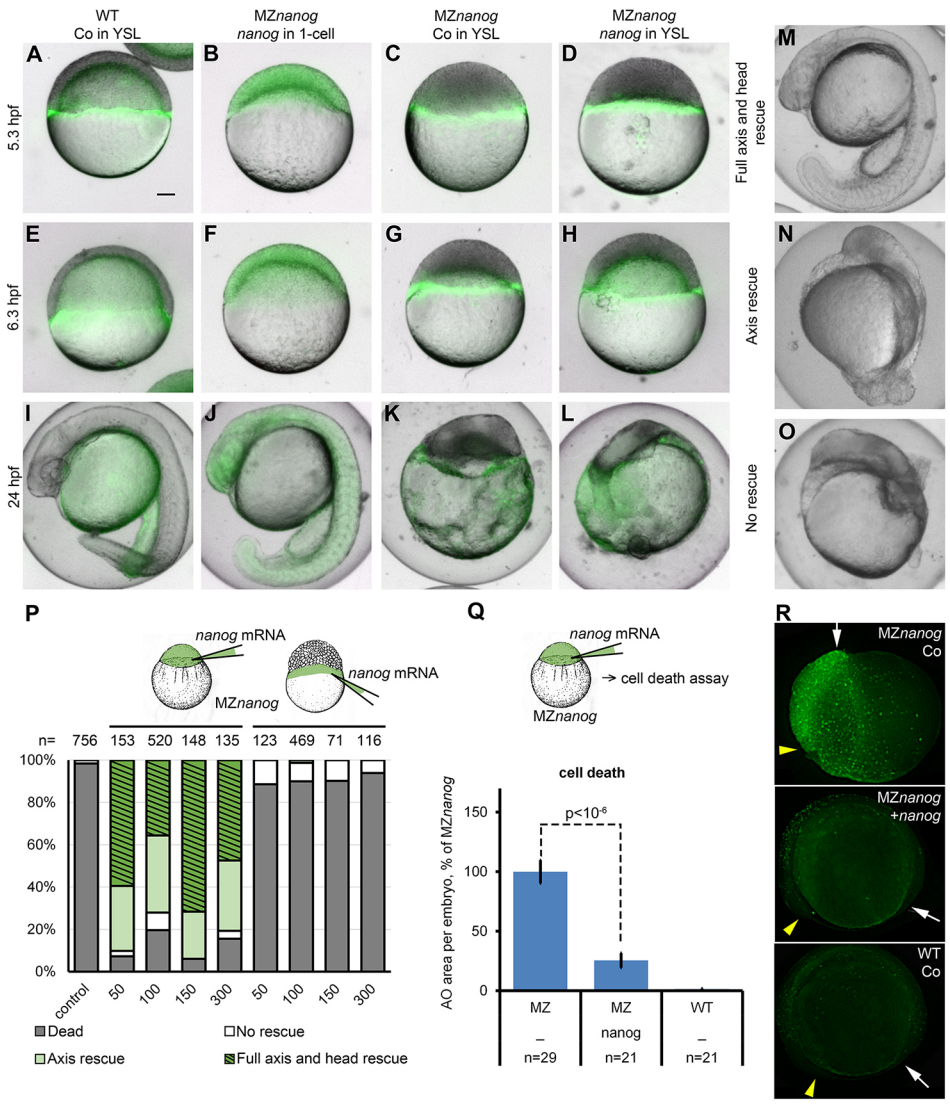

Fig. 5. *nanog* mRNA injection at 1-cell stage completely rescues MZ*nanog* embryos. (A-L) Representative embryo phenotypes from a single rescue experiment: *nanog* mRNA or control (Co) mRNA, as indicated, was co-injected with Alexa 488 dextran (green) in the YSL (A,C-E,G-I,K,L) or in 1-cell stage (B,F,J) of wild-type (WT; A,E,I) or MZ*nanog* (B-D,F-H,J-L) embryos. Live images in differential interference contrast and green fluorescence were taken at indicated stages. (M-O) Phenotypic classes used for scoring the rescued phenotypes at 24 hpf. (P) Rescue statistics after 24 hpf. Concentrations of *nanog* mRNA are indicated below the graph in pg per embryo. Numbers of embryos from two experiments are indicated above the bars. Schematics indicate the injection protocol. (Q,R) *nanog* mRNA injection at the 1-cell stage rescues cell death of MZ*nanog*. MZ*nanog* embryos were injected with *nanog* mRNA at 1-cell stage or not injected (–; Co) and stained at 9 hpf with Acridine Orange to detect and score dead cells. (Q) Dead cells rescue statistics: *nanog* mRNA injection significantly reduces cell death in MZ*nanog* ($P<10^{-6}$, Student's *t*-test); *n*, number of scored embryos. Error bars represent s.e.m. (R) Groups of dead cells in MZ*nanog* control, MZ*nanog nanog*-injected embryos and WT, as indicated. Embryos shown at 12 hpf. Yellow arrowheads and white arrows point to anterior and posterior ends or dorsal embryo axes, respectively. Scale bar: 100 µm (A-O).

the survival rates of *mxtx2* mRNA- and miR-430-injected embryos were poor (Fig. 6E, see figure legend for details). To investigate whether epiboly rescue by *mxtx2 or* miR-430 occurs using the same molecular mechanisms, we performed *in situ* hybridization for Nodal pathway targets *sox32* and *sox17* on MZ*nanog* embryos injected with *nanog*, *mxtx2* or miR-430 at the 1-cell stage (Fig. 6G,H, Table S2). miR-430 injection did not have any effect on *sox32* and *sox17*, whereas *nanog* injection resulted in a moderate increase of scattered *sox32*- and *sox17*-positive cells compared with MZ*nanog* control. *mxtx2* injection to MZ*nanog* resulted in the appearance of supernumerous clustered *sox32*- and *sox17*-positive cells (Fig. 6G,H), indicating excessive endoderm formation even when compared with the wild-type control (Fig. S7). The elevated *eomesa* expression in *MZnanog* mutants at midgastrula stages (see Fig. 3G) could be rescued by miR-430 but not by mismatch control microRNA injection (Fig. 6I, Table S2). Therefore, we assumed that the delay in maternal mRNA degradation, caused by the absence of miR-430, contributes to the epiboly defect in MZ*nanog*.

Nanog is necessary for expression of ventral-specifying genes in the ectodermal domain

Using Nanog KD experiments, Perez-Camps and colleagues have recently suggested a role for Pou5f3-Nanog complexes in patterning the dorsoventral axis (Perez-Camps et al., 2016). We checked whether the effects of Nanog KD on the expression of dorsoventral markers could be reproduced in MZ*nanog*. We took the maternal-zygotic Pou5f3 mutant MZ*spg*^{m793} for comparison, in which the deficiency of ventral-specifying genes has been previously documented (Reim and Brand, 2006; Belting et al., 2011). We did not observe expansion of the dorsal genes *chordin* (*chrd*) and *gsc* (Fig. 7A,B,F,G,K,L), but transcription of *vox* and *vent* was more prominently downregulated in MZ*nanog* than in MZ*spg* (compare Fig. 7H,I with 7M,N, and Fig. S8A,C,E). Remarkably, *bmp2b* and *vox* expression in the ectodermal domain was completely absent in MZ*nanog*, but only reduced in MZ*spg* (Fig. 7E,J,O; see also Fig. S8B,D,F). This result is in agreement with the cooperative action of Pou5f3 and Nanog in ventral mesoderm (Perez-Camps et al., 2016) and suggests an additional role for Nanog in establishing ventral domains of *bmp2b* and *vox* in the ectoderm. In support of this idea, BMP-mediated repression of SoxB1 neural genes at the ventral side of the ectoderm (Dee et al., 2007) does not occur in MZ*nanog* (Fig. S9A).

Nanog represses a direct zygotic target of Pou5f3, the neural gene *her3*

To characterize further the interactions between Pou5f3 and Nanog gene regulatory networks, we investigated the effects of Nanog on

Development (2018) 145, dev155366. doi:10.1242/dev.155366

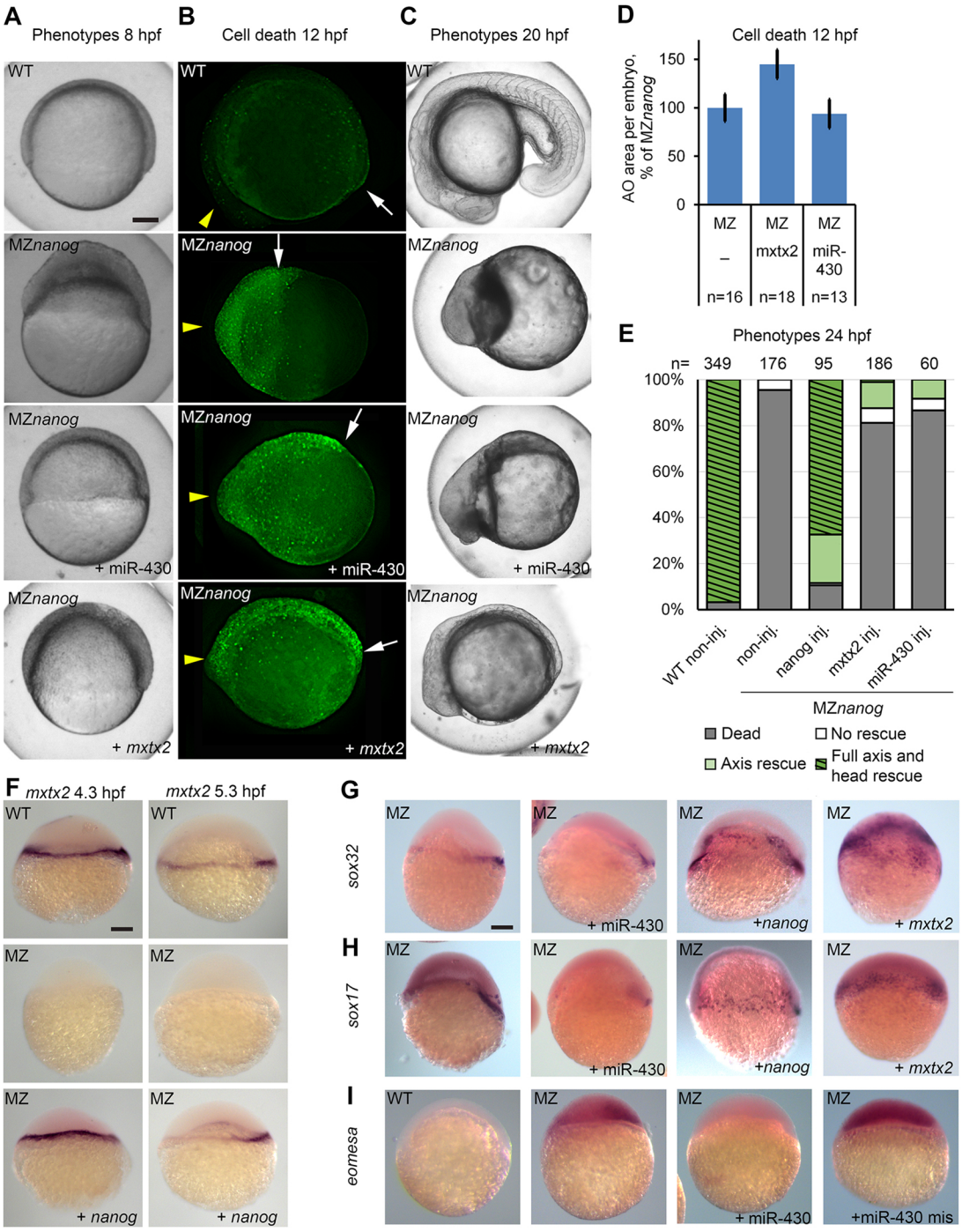

Fig. 6. *mxtx2* or miR-430 injection at the 1-cell stage rescues epiboly but not cell death in MZ*nanog* embryos. (A-C) MZ*nanog* embryos were injected at the 1-cell stage with *mxtx2* mRNA or miR-430, as indicated, or not injected. Wild-type (WT) embryos were used as stage control. (A) Representative phenotypes at 8 hpf. Note the thinning of blastoderm and epiboly progression in injected MZ*nanog* embryos compared with non-injected MZ*nanog*. (B) Staining for dead cells in 12 hpf embryos. Yellow arrowheads and white arrows point to anterior and posterior ends of embryo axes, respectively. (C) Representative phenotypes at 20 hpf. (D) Dead cells rescue statistics: neither *mxtx2* nor miR-430 mRNA injection reduced cell death in MZ*nanog*; *n*, number of scored embryos. Error bars represent s.e.m. (E) Phenotype rescue statistics after 24 hpf. One-cell stage MZ*nanog* embryos were injected as indicated or left non-injected; classes used for scoring are shown in Fig. 5M-O. Numbers of embryos are indicated above the bars. (F-I) *In situ* hybridization for *mxtx2* at 4.3 and 5.3 hpf (F), *sox32* at 8 hpf (G), *sox17* at 8 hpf (H) and *eomesa* at 6 hpf (I). Genotypes are indicated top left as MZ (MZ*nanog*) or WT, injected substances are indicated bottom right. Lateral views. Scale bars: 100 µm.

Pou5f3 bona fide direct transcriptional regulatory targets. Pou5f3 is absolutely required for early zygotic expression of the transcription factors *sox2*, *her3* and *foxd3* (Onichtchouk et al., 2010; Iwafuchi-Doi et al., 2011). Expression of *foxd3* (Fig. 3C, Fig. S3) and *sox2* (Fig. S9B,C) was not strongly affected in MZ*nanog* mutants. Expression of the strictly zygotic gene *her3* first becomes visible in the future neuroectoderm at 4.7 hpf in the wild type (Hans et al., 2004; Bae et al., 2005). Unexpectedly, *her3* was strongly increased at 4.7 hpf and expanded throughout the blastoderm of MZ*nanog* (Fig. 7P). We have previously shown that accumulation of *her3* transcripts over

Development (2018) 145, dev155366. doi:10.1242/dev.155366

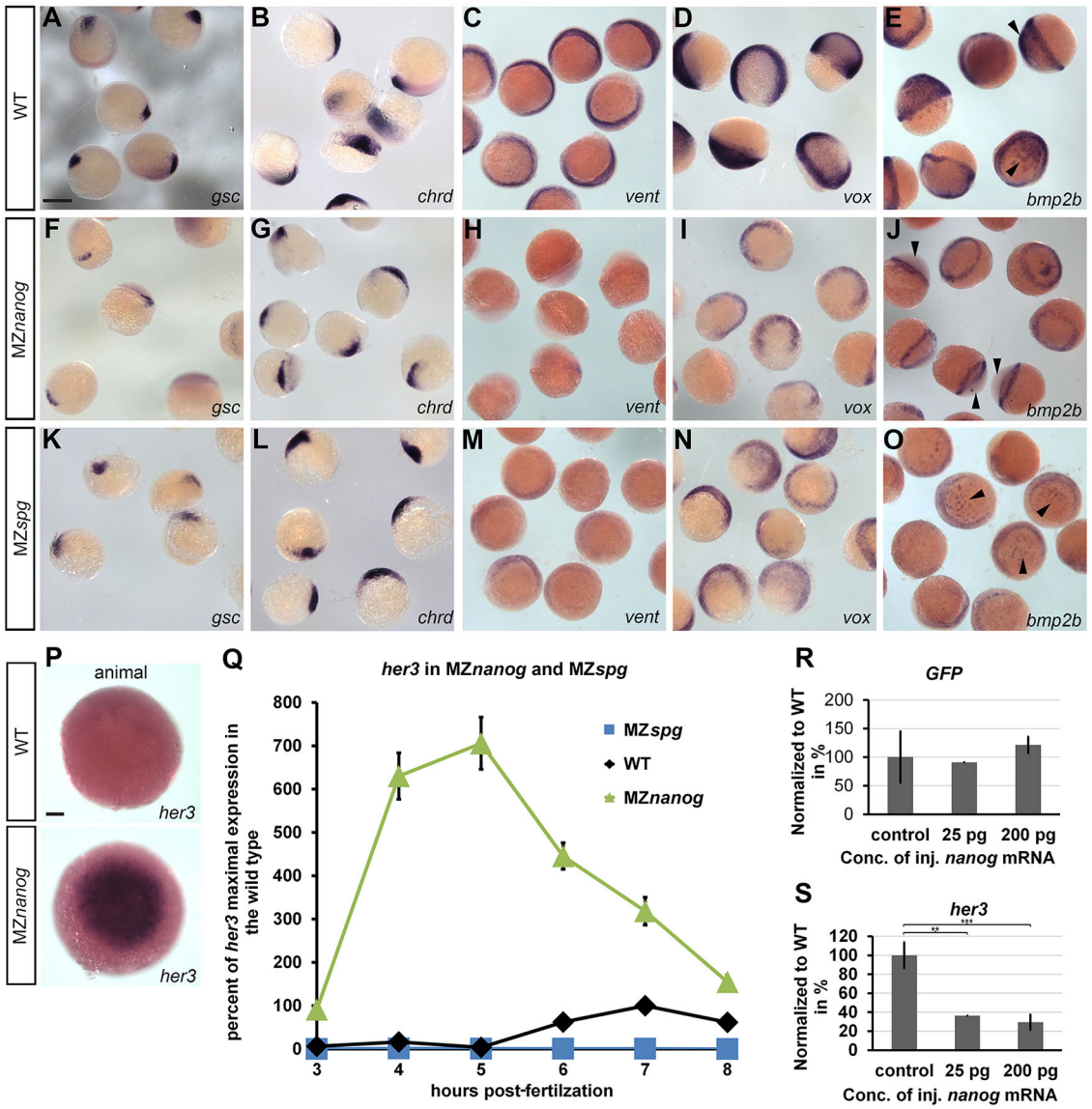

Fig. 7. Nanog is required for the expression of the ventral genes *bmp2b*, *vox* and *vent* and for the proper expression levels of the neural gene *her3*. (A-O) *In situ* hybridization for dorsal- and ventral-specifying genes was performed in parallel using wild type (WT), MZ*nanog* and MZ*spg* at the shield stage. The dorsal markers *gsc* (A,F,K) and *chrd* (B,G,L) are slightly reduced in MZ*nanog* embryos. *vent* expression (C,H,M) is not detectable in MZ*nanog* but is visible although reduced in MZ*spg*. *vox* (D,I,N) and *bmp2b* (E,J,O) expression is reduced in the mesoderm and missing from the ectoderm of MZ*nanog* (arrowheads), whereas in MZ*spg* expression in both tissues is reduced, but detectable. (P) *In situ* hybridization at 4.7 hpf for *her3* in WT and MZ*nanog* (animal view). At this stage, *her3* in the WT is expressed in presumptive neural ectoderm (Hans et al., 2004). Because of the upregulation in the MZ*nanog* mutant, the staining reaction was stopped before this staining was visible. (Q) *her3* time curve generated by quantitative real-time PCR on WT, MZ*nanog* and MZ*spg*. Embryos were collected at 1 h intervals from 3 hpf to 8 hpf. All expression values were normalized to *her3* maximal expression in WT (7 hpf). Error bars represent s.d.; *n*=3. (R,S) Overexpression of Nanog in Tg(*her3enh1-GFP*) embryos changes *her3* levels. We injected *nanog* or control mRNA in Tg(*her3enh1-GFP*) transgenic embryos at the 1-cell stage and performed quantitative RT-PCR on shield stage-embryos measuring changes of *her3* and *GFP* RNA levels. Overexpression of Nanog did not change *GFP* levels (R) but repressed endogenous *her3* (**P<0.001, ***P<1*E^{-05}, Student's *t*-test) (S). Error bars represent s.d., *n*=3. Scale bars: 700 µm (A-O); 100 µm (P).

time follows a biphasic pattern, where low levels of *her3* transcription start at ZGA (3 hpf) and increase to high levels prior to shield stage (6 hpf; Onichtchouk et al., 2010). To investigate whether this temporal pattern is affected in the absence of Nanog, we obtained a *her3* expression time curve using quantitative RT-PCR on wild-type, MZ*nanog* and MZ*spg* embryos, respectively (Fig. 7Q). Strikingly, already at ZGA the expression level of *her3* in MZ*nanog* was ten times greater than the *her3* wild-type control level. It further increased sharply and reached a maximum at 5 hpf. Expression time curves of the SoxB1 family neural genes *sox2*, *sox3* and *sox19a* did not show similar dramatic changes in MZ*nanog* (Fig. S9C). Thus, we concluded that *in vivo* Nanog acts as a potent direct or indirect repressor of *her3*. Pou5f3 activates *her3* transcription by binding upstream of the *her3* promoter (Onichtchouk et al., 2010). In order to investigate whether Nanog repression is mediated by the same genomic region, we made use of the Tg(*her3enh1-GFP*) transgenic reporter line, in which expression of GFP is regulated by 2.2 kb of *her3* upstream sequence. This sequence harbors a conserved Pou5f3-binding regulatory site directly upstream of the TATA box (Onichtchouk et al., 2010). We microinjected Nanog or control

Development (2018) 145, dev155366. doi:10.1242/dev.155366

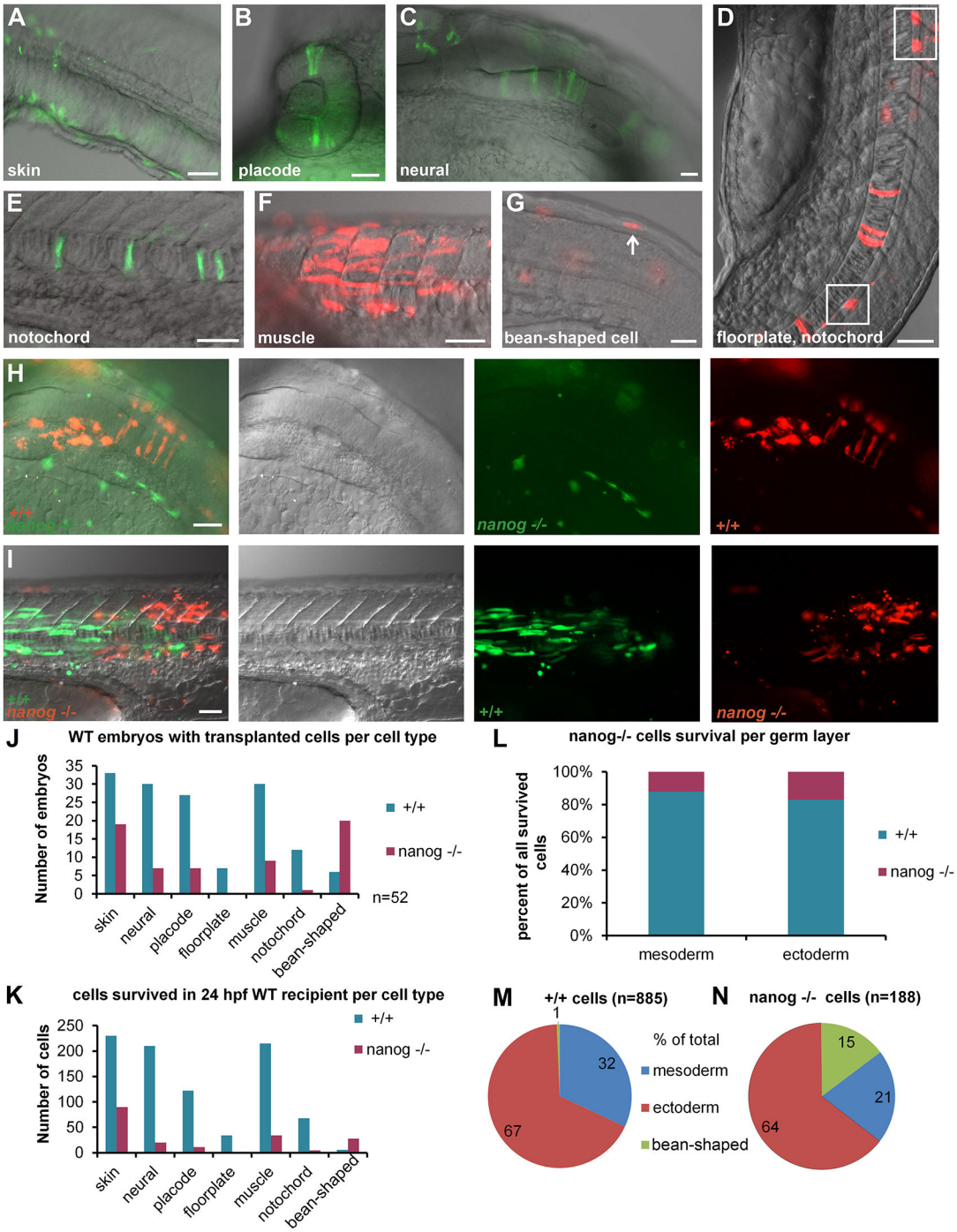

Fig. 8. Transplantation experiment reveals cell-autonomous death of *nanog*$^{-/-}$ cells. (A-G) Scored cell types: skin cells (A), placode, e.g. eye (B), neural epithelial cells in the hindbrain (C), floorplate cells (D), cells in the notochord (E), muscle cells (F), non-specified 'bean-shaped' cells (G). Anterior is always to the right, except in D in which anterior is toward the top. (H,I) Two examples of differentiated co-transplanted wild-type (+/+) and *nanog*$^{-/-}$ cells in 24 hpf wild-type (WT) host. Overlay, differential interference contrast, green and red channels from left to right. (H) Neural tissue: *nanog*$^{-/-}$ cells (green) differentiated as skin and +/+ cells (red) contributed to neural epithelium in the hindbrain region of the 24 hpf WT host. (I) Trunk muscles: 6 *nanog*$^{-/-}$ (red) muscle fibers and 27 +/+ (green) muscle fibers are visible. (J) Number of embryos with at least one transplanted cell per cell type for +/+ and *nanog*$^{-/-}$ cells in 52 hosts (note that the embryos which contained several types of donor cells were scored more than once). (K) Total number of transplanted cells per tissue in 52 hosts. *P*-values for the difference between the numbers of +/+ and *nanog*$^{-/-}$ cells were significant for all tissues ($P<0.01$, paired *t*-test; see also Table S3). (L) Percentage of surviving cells separated by germ layer: mesoderm (muscle and notochord) and ectoderm (skin, neural cells, placodes and floorplate cells). Contribution of *nanog*$^{-/-}$ cells to both mesodermal and ectoderm derivatives was <20%. (M,N) Distribution of +/+ and *nanog*$^{-/-}$ cells between mesodermal and ectodermal tissue and non-specified 'bean-shaped' cells. Scale bars: 40 µm (A,C-G,I); 200 µm (B); 100 µm (H).

mRNA in Tg(*her3enh1-GFP*) embryos at the 1-cell stage, harvested the embryos at 6 hpf and measured the changes of endogenous *her3* RNA and *GFP* by quantitative RT-PCR. Whereas overexpression of Nanog did not change *GFP* levels (Fig. 7R), levels of endogenous *her3* RNA (Fig. 7S) were significantly downregulated by both concentrations injected. We concluded that Nanog represses *her3* by

Development (2018) 145, dev155366. doi:10.1242/dev.155366

using regulatory sequences outside of the 2.2 kb upstream DNA element.

Nanog cell-autonomously contributes to cell survival within developing embryos

Cell death, observed in MZ*nanog* mutants at the end of gastrulation, could either result from a cell-autonomous requirement for Nanog or from the absence of important extracellular or extra-embryonic signals in the MZ*nanog* embryo. To determine whether Nanog is cell-autonomously required for cell survival, we performed a series of transplantation experiments of labeled wild-type and MZ*nanog* donor cells to the unlabeled wild-type host. Both donors and host were at the blastula stage (sphere, 4 hpf). At this early stage, cells are considered to be pluripotent (Ho and Kimmel, 1993). First, in a set of preliminary experiments, we transplanted labeled wild-type cells into wild-type recipients and examined them after 24 hpf, to define which cell types are easily recognizable and abundant enough to score (see Materials and Methods). By cell shape and position within the 24 hpf embryo, we could reliably distinguish seven cell type groups: four groups of ectoderm derivatives (skin, neural, placode, floorplate; Fig. 8A-D), two groups of mesoderm derivatives (muscle and notochord; Fig. 8E,F) and one group of undefined origin, which comprised singular bean-shaped cells, positioned directly underneath the embryonic epidermis (Fig. 8G). We then addressed the possible cell-autonomous differences between MZ*nanog* and wild-type cells by co-transplanting cells of both genotypes labeled with different fluorescent colors into an unlabeled wild-type host at the sphere stage (52 host embryos were transplanted in ten experiments). The fluorescent cells in the 24 hpf host embryos that matched to one of the defined seven cell types were scored. The order of transplantation and color of labeling dextran was alternated between wild-type and MZ*nanog* cells to avoid experimental bias (see Materials and Methods and Table S3 for details).

Although MZ*nanog* precursors did contribute to six out of seven cell types, this contribution was much smaller than that of the wild-type precursors (Fig. 8H,I). For all cell types except the undefined bean-shaped ones, more host embryos carried derivatives of wild-type than of MZ*nanog* precursors (Fig. 8J). The total number of cells (885) derived from the wild-type precursors exceeded by more than four times the number of MZ*nanog* derivatives (188). Wild-type cells were more abundant than MZ*nanog* cells within all categories of cell types, except bean-shaped cells (Fig. 8K). The differences between MZ*nanog*- and wild type-derived cells per host embryo were statistically significant in all categories: *P*-values in paired Student's *t*-test varied from $5.2E^{-7}$ (neural) to 0.024 (floorplate) and the *P*-value for the increase in bean-shaped cells in MZ*nanog* was 0.000101 (Table S3). In summary, MZ*nanog* precursors contributed to <20% of mesodermal (muscle and notochord) or ectodermal (skin, neural, placode and floorplate) cell types (Fig. 8L). Finally, we estimated the cell type distribution within all differentiated cells within each genotype (Fig. 8M,N). Whereas non-defined bean-shaped cells were scored as <1% (0.67%) of all wild-type cells, they represented 15% of all MZ*nanog* cell derivatives. We hypothesize here that the bean-shaped cells are simply remnant transplanted blastula cells. They did not divide further (thus stayed big) and also did not differentiate. It is possible that they might become stuck below the EVL/skin because of adhesion problems.

DISCUSSION

Genomic studies and transcriptome analyses (Xu et al., 2012; Lee et al., 2013) revealed a broad range of Nanog genomic binding sites and transcriptionally regulated targets in zebrafish, suggesting that Nanog contributes to multiple developmental processes. However, the extent to which Nanog might contribute in specific, non-redundant ways to biological regulation was remained controversial.

Here, we investigated the cell-autonomous and non-cell autonomous requirements for Nanog in embryonic (deep cells) and extra-embryonic (YSL and YCL) tissues using maternal-zygotic mutant MZ*nanog* embryos. Taken together, these findings suggest that Nanog influences diverse developmental processes, and interferes with more than one signaling cascade. The pleiotropic action of Nanog resembles that of Oct4/Pou5f3 (summarized in Fig. 9).

Nanog affects the architecture of the yolk extra-embryonic layer by *mxtx2*-dependent and *mxtx2*-independent mechanisms

The YSL nuclei migration defect and the deficiency of the F-actin ring in MZ*nanog* embryos resemble the phenotype described for Mxtx2 morphants (Wilkins et al., 2008). However, the yolk burst phenotype observed in 100% of Mxtx2 KD embryos was not readily apparent in MZ*nanog* (Fig. 1C, Fig. 4O,P). Additionally, yolk doming (Fig. 4K-N) and YCL microtubule organization (Fig. 4R,S) were abnormal. Injection of *mxtx2* mRNA into the YSL at the 512-cell stage did not rescue epiboly in MZ*nanog* (Fig. S5), strongly suggesting that the absence of *mxtx2* can only partially explain the severe yolk cell phenotype of MZ*nanog* mutants.

Previous studies revealed that Mxtx2 is strictly required only in the YSL (Bruce et al., 2005; Wilkins et al., 2008). Therefore, the rescue of MZ*nanog* by 1-cell stage injection of *mxtx2* mRNA (Fig. 6A-C) is somewhat puzzling. In addition to restoring normal Mxtx2 function in the YSL, Mxtx2 was misexpressed in the deep cells, where it is normally not present. As found previously (Xu

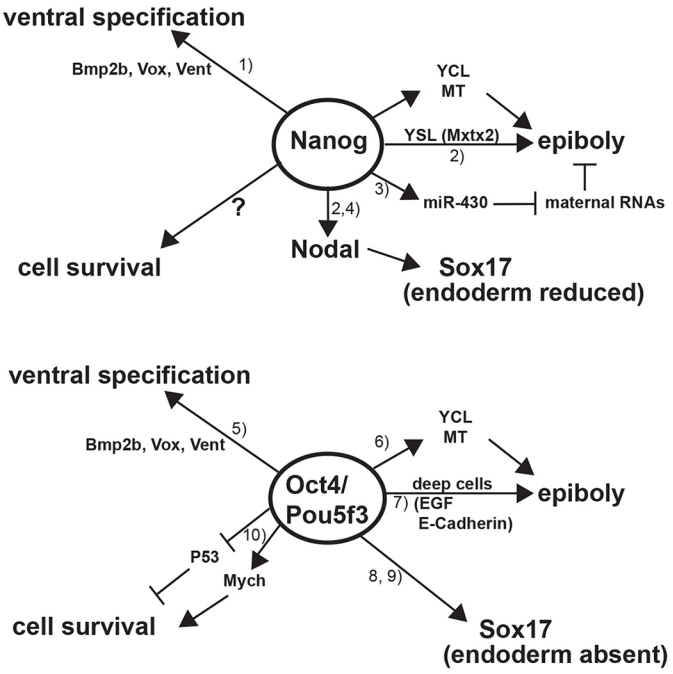

Fig. 9. Common processes regulated by Nanog and Oct4/Pou5f3. Nanog and Oct4/Pou5f3 regulate ventral specification, epiboly, cell survival and endoderm formation. There are both common and distinct mechanisms underlying the action of Nanog and Oct4/Pou5f3 in each case. See Discussion for details. References: (1) Perez-Camps et al., 2016; (2) Xu et al., 2012; (3) Lee et al., 2013; (4) Gagnon et al., 2018; (5) Reim and Brand, 2006; (6) Lachnit et al., 2008; (7) Song et al., 2013; (8) Lunde et al., 2004; (9) Reim et al., 2004; (10) Kotkamp et al., 2014.

Development (2018) 145, dev155366. doi:10.1242/dev.155366

et al., 2012), Mxtx2 genomic binding sites largely overlap with Nanog-binding sites. One can therefore speculate that Mxtx2 might directly activate Nanog target genes when overexpressed. Another possible explanation for Mxtx2-mediated rescue of MZ*nanog* is the ability of Mxtx2 to activate Nodal signaling (Hong et al., 2011; Xu et al., 2012). Motile and adhesive endodermal cells migrate to the interface of blastoderm and yolk and spread by random walk movement (Warga and Nüsslein-Volhard, 1999; David and Rosa, 2001). Mxtx2 induces supernumerous endoderm cells in MZ*nanog* (Fig. 6G,H, Fig. S7). Their properties might artificially compensate for MZ*nanog* epiboly defect. In any case, rescue of MZ*nanog* by *mxtx2* injection into 1-cell stage embryos is based on an ectopic overexpression artifact. The yolk cell phenotype in MZ*nanog* is likely caused by a combination of two or more independent defects: abnormal microtubule structures, the absence of Mxtx2 and its target genes and, presumably, also excessive maternal mRNA accumulation in the yolk cell.

Nanog activation of miR-430 contributes to proper deep cell epiboly

Nanog directly activates transcription of miR-430 (Lee et al., 2013), which is in charge of mRNA clearance for a large group of maternal transcripts after ZGA (Giraldez et al., 2006). Zebrafish MZ*dicer* mutants, in which the whole microRNA processing pathway is inactive, show strong epiboly delay without affecting axis formation or other gastrulation movements (Giraldez et al., 2005). Accumulation of non-degraded maternal transcripts contributed to epiboly delay in MZ*nanog*, as miR-430 overexpression in the whole embryo significantly improved epiboly (Fig. 6A, Fig. S6). Experiments performed by Gagnon et al. (2018) demonstrate that MZ*nanog* blastoderm transplanted to the wild-type yolk completes epiboly, thus tolerating excessive maternal RNA load in the deep cells. By contrast, our miR-430 rescue shows that just removing maternal mRNA load from intact embryo allows the MZ*nanog* embryo to pass through epiboly in spite of severe yolk cell defects. One cannot exclude the possibility that the absence of miR-430-mediated mRNA degradation in the yolk cell of MZ*nanog* also contributes to the mutant yolk cell phenotype, which would explain the results of both papers. In addition, the morphology of EVL surface cells apparently differs between wild type and MZ*nanog* (Fig. 4O,P, Fig. S4); thus, abnormal EVL in MZ*nanog* might also contribute to doming defects (Morita et al., 2017), although this possibility needs further investigation. From all available data, we can conclude that multiple factors contribute to epiboly failure in MZ*nanog*.

Reduced survival of MZ*nanog* cells is independent of gastrulation defects

We demonstrate that MZ*nanog* mutants show increased cell death at the end of gastrulation (Fig. 2). We have shown in a cell transplantation assay that survival of selected morphologically defined cell lineages – muscle, neurons, skin and placodes – is reduced in MZ*nanog* compared with wild-type cells, and survival of all cell types seems to be equally diminished (Fig. 8). This cell-autonomous phenotype could be rescued only by supplementing *nanog* mRNA or by a paternal *nanog* wild-type allele in M*nanog*, but not by miR-430 microinjection or by ectopic overexpression of Mxtx2 (Fig. 6). Transplantation results of GFP transgenic M*nanog* heterozygous cells, as performed by Gagnon et al. (2018), taken together with our MZ*nanog* cell transplantation results, demonstrate that *nanog* is not absolutely required for cell differentiation into specific lineages. Rather, it is needed for cell viability and robustness of lineage specification. The 'bean-shaped cells' in our experiments might represent a cell type that appears only upon transplantation (their shape fits that of blastoderm cells). Despite many developmental signals, they remain undetermined and may develop no adhesion profile to fit into tissues. Although it is generally believed that in mammals Nanog is mostly dispensable after pluripotency is established, mouse Nanog mutant ESCs also have reduced viability and differentiation capacity compared with wild-type ESCs (see figure 1F in Chambers et al., 2007), resembling zebrafish MZ*nanog* cells.

Comparison of MZ*nanog* and MZ*spg* mutant phenotypes highlights pleiotropic and specific actions of Nanog and Oct4/Pou5f3 transcription factors

MZ*nanog* and Pou5f3 (Oct4 paralogous) MZ*spg* mutant embryos are similar in some aspects of their phenotype, such as epiboly delay, misregulation of ventral genes, and enhanced cell death at the end of gastrulation, but differ in other aspects, such as the ability to form *sox17*-positive endoderm (illustrated in Fig. 9). Both transcription factors contribute to epiboly by regulating the YCL microtubule cytoskeleton (Fig. 4R-S′). Other known pathways involved in epiboly regulation rely on different target genes and mechanisms downstream of Pou5f3 (Song et al., 2013) and Nanog. In contrast to MZ*nanog*, *mxtx2* expression is not changed in MZ*spg* (Onichtchouk et al., 2010), and YSL epiboly occurs relatively normally (Lachnit et al., 2008). Nanog and Oct4/Pou5f3 synergize with the ventral specification pathway via BMP signaling and Vox (Peres-Camps et al., 2016; this study). Pou5f3 regulates cell survival by inhibiting *p53* (*tp53*) and activating *mych* (Kotkamp et al., 2014). The decrease in cell survival, observed in both Nanog and Oct4/Pou5f3 mutants, could be caused by multiple independent changes due to a widespread role of Nanog and Pou5f3 in gene expression. Although each of these changes is not essential for cell survival, the multiple changes add up, providing an effect which reduces the robustness and viability of cells.

It is known that Nanog and Oct4 often co-occupy the same regulatory sequences to directly activate gene expression (Boyer et al., 2005; Lee et al., 2013). However, this does not appear to be the case for all Nanog/Oct4 target genes. We show regulation of *her3* as an example of antagonistic regulation by Pou5f3 and Nanog: *her3* is activated by Pou5f3 (Onichtchouk et al., 2010), and strongly repressed by Nanog (Fig. 7P,Q). We further show that Pou5f3 and Nanog use different *her3* regulatory regions (Fig. 7R,S).

Taken together, our data suggest that Nanog, similarly to Oct4/Pou5f3, controls expression of a large network of developmentally important signaling molecules and transcription factors.

MATERIALS AND METHODS

Zebrafish maintenance and embryo care

Fish were raised, maintained and crossed under standard conditions as described by Westerfield (2000). Embryos obtained from crosses were raised in egg water at 28.5°C. Developmental stages of MZ*spg* and MZ*nanog* embryos were indirectly determined by observation of wild-type embryos born at the same time and incubated under identical conditions. For controls, we used the AB-TL wild-type embryos. Staging was performed following the 1995 Kimmel publication (Kimmel et al., 1995). All experiments were implemented in accordance with German Animal Protection Law (TierSchG).

nanog TALEN mutagenesis

For *nanog* mutant generation, we followed the published protocol of Cermak et al. (2011). Using Mojo hand on the website www.talendesign.org/ (Neff et al., 2013), we created the TALENs targeting the codon encoding the 12th amino acid of the first exon of the *nanog* gene (spacer sequence is indicated by square brackets, flanking TAL1 and TAL2):

Development (2018) 145, dev155366. doi:10.1242/dev.155366

5′-TTTAACCCATCTTATC[ATGCATATGCATACG]GGCTCATGTA-CCCGCA-3′ (according to assembly Jul. 2010, zv9/danRer7, chr24:12,738,352-12,738,398).

The targeting site contains the restriction site (5′-CATATG-3′) for the enzyme *Nde*I (NEB), which cuts between CA and TATG. For assembling the correct RVDs, we used the Golden Gate TALEN and TAL Effector Kit 2.0 (Kit #1000000024, Addgene), which includes all plasmids needed. As a destination vector we chose the pRCIscript-Goldy TALEN (Addgene plasmid #38142, deposited by Daniel Carlson; Carlson et al., 2012). After successfully generating the two TALEN plasmids, we performed RNA transcription with the mMESSAGE mMACHINE T3 Transcription Kit (Ambion) followed by injection of RNA into AB-TL wild-type embryos at the 1-cell stage to the yolk with a concentration of 100 ng/µl for each TALEN-RNA. To check the proper functioning of the TALENs, we extracted genomic DNA from 20 each of 24 hpf wild-type and injected embryos by lysing the cells with lysis buffer (10 mM Tris pH 8, 50 mM KCl, 0.3% Tween20, 0.3% NP-40, 1 mM EDTA) and incubating the embryos at 98°C for 10 min. After cooling down, Proteinase K solution (20 mg/ml, A3830, AppliChem) was added and incubated overnight or at least 2 h at 56°C. Subsequently, Proteinase K was destroyed by heating the samples to 98°C for 10 min. For PCR, we designed primers flanking the targeting site: Nanog-f1 5′- TCTAAACCCGCCCACAACC-3′ and Nanog-r1 5′-GGTCGGGCTCAGTCTTGTTG-3′ resulting in a 523 bp product. After digestion with *Nde*I (overnight, 37°C) fragments of 284 and 238 bp lengths were generated in the case that no mutation had taken place. In more than 70% of *nanog* TALEN-injected single G0 embryos an undigested DNA band could be detected, indicating high efficiency of mutagenesis. Eleven out of 19 tested G0 mosaic fish transmitted the mutation to the F1 generation. Two of G0 *nanog* TALEN-injected mosaic female founders, when crossed to wild-type males, generated abnormal embryos phenotypically resembling morpholino KD Nanog phenotypes (Xu et al., 2012), which we interpreted as a bi-allelic targeting of the gene. We selected a founder carrying the 10 bp deletion (5′-TTTAACCCATCTTATCAT|ACGGGCTCATGTACCCGCA-3′; the line shows the position of the missing base pairs), which caused a frame shift and a premature stop codon after 15 amino acids (Fig. 1A), for further experiments. Resulting F2 homozygous *nanog* mutants developed into fertile adults, suggesting that Nanog zygotic contribution is not essential for development.

Whole-mount *in situ* hybridization (WISH)

To visualize the expression pattern of some chosen genes, we performed whole-mount *in situ* hybridization as previously described (Holzschuh et al., 2003), with some modifications. Embryos were fixed at the appropriate stages with 4% paraformaldehyde (PFA) at 4°C overnight. The next day, the fixed embryos were washed thrice in PBST (8 g/l NaCl, 0.2 g/l KCl, 16 mM Na_2HPO_4, 4 mM NaH_2PO_4, 0.1% Tween-20, pH 7.3) for 5 min and were dechorionated. The dechorionated embryos were dehydrated in stepwise increasing concentrations of methanol (25%, 50%, 75% in PBST, finally in 100%) and were stored in 100% methanol at −20°C until further use. The sources of the probes used for *in situ* hybridization are listed in Table S5. To create the plasmid templates for *eomesa*, *mxtx2* and *sox19a*, corresponding partial open reading frame sequences were PCR-amplified using cDNA from 4-6 hpf embryos and primers listed in the Table S6. PCR products were then cloned into PCRII TOPO vector (Invitrogen).

Day 1

The embryos were rehydrated in stepwise decreasing concentrations of methanol (75%, 50% and 25% in PBST), each 5 min on a shaker. Subsequently, they were washed three times in PBST. Afterwards, the embryos were transferred into 300 µl Hyb-Mix (50% formamide, 5× SSC, 50 µg/ml heparin sodium salt, 0.1% Tween-20, 5 mg/ml torula RNA) and incubated for 4 h at 65°C. For hybridization, the Hyb-Mix was replaced by 300 µl Hyb-Mix containing the desired probe (0.5-2.0 µl/100 µl) and incubated overnight at 65°C.

Day 2

The probes were removed and the embryos were transferred into a 48-well plate with a net as bottom and placed into the *in situ* robot BioLane HTI using program HL2_3. The robot washed the embryos thrice with 50% formamide in 2× SSCT (20× SSC: 3 M NaCl, 300 mM trisodium citrate; 2× SSCT and 0.2× SSCT contain the corresponding SSC strength together with 0.1% Tween-20) for 20 min, then once with 2× SSCT for 15 min and thereafter thrice with 0.2× SSCT for 20 min. All steps were carried out at 65°C.

The next steps were performed at room temperature (RT). The embryos were washed twice with PBST for 10 min and subsequently incubated for 2 h in blocking solution [2% heat-inactivated goat serum, 2 mg/ml bovine serum albumin in PBST]. After blocking, the samples were incubated with an anti-digoxigenin antibody (1:5000 in PBST; Roche Diagnostics, 11 093 274 910) overnight at 4°C.

Day 3

Embryos were rinsed once in PBST and then washed six times in PBST for 20 min each wash. Afterwards, they were washed for 10 min in 100 mM Tris-HCl pH 9.5. The embryos were then removed from the robot and transferred into 12-well plates and incubated in staining buffer (100 mM NaCl, 50 mM $MgCl_2$, 100 mM Tris-HCl pH 9.5, 0.1% Tween-20, 1 mM levamisole) for 15 min. For staining, the staining buffer was replaced with staining solution [per 1 ml staining buffer 3.5 µl BCIP (stock solution 50 mg/ml in 100% DMF) and 3.5 µl NBT (stock solution 50 mg/ml in 100% DMF)] and incubated in the dark on a shaker until a proper coloring developed. Unbound dye was removed by washing six times with stop solution for 20 min or even longer. For storage, the embryos were moved through incubations in solutions with an increasing concentration of glycerol (25%, 50% and 75% in stop solution) until 90% glycerol in stop solution (PBST pH 5.5, 1 mM EDTA), at which point the embryos sank down and then were placed to 4°C storage. Following this, images were recorded with a Leica MZ APO stereo microscope, an AxioCam MRc camera and AxioVS40 V4.8.0.0 software (Zeiss).

microRNA and mRNA synthesis

miR-430 and mismatch control microRNAs were synthesized as described by Giraldez et al. (2005). The *nanog* and *mxtx2* mRNA for rescue experiments were synthesized using the SP6 Ambion mMessage Machine kit according to the manufacturer's instructions. CS2+*nanog* and CS2 +*mxtx2* plasmids were linearized by *Not*I and used as templates.

Microinjections

The wild-type and MZ*nanog* eggs for all injections were collected within 10 min. YSL injections were performed according to D'Amico and Cooper (2001) at the 512- to 1000-cell stage. For 1-cell stage and YSL injections, in addition to injected mRNA or microRNA we used a dextran conjugated to Alexa Fluor 488 or tetramethylrhodamine (Thermo Fisher Scientific, 12.5 ng per embryo) to visualize the YSL or embryonic cells. Just after YSL injection, the embryos were visually examined under an epifluorescence microscope, and the mis-injected (30-60%) embryos showing fluorescence in the deep cells or in the yolk were excluded from the follow-up experimental analyses. For transplantation experiments, dextran Alexa Fluor 488 or tetramethylrhodamine dextran (Thermo Fisher Scientific) were injected at the 1-cell stage at a concentration of 12.5 ng per embryo. For the rescue of MZ*nanog* embryos, we performed *nanog* mRNA injections into MZ*nanog* mutant embryos with amounts of 50 pg, 100 pg, 150 pg and 300 pg per embryo. Use of 150 pg per embryo usually resulted in the healthiest embryos when injected at the 1-cell stage. *mxtx2* mRNA injections into 1-cell stage MZ*nanog* mutant embryos were performed with amounts of 6 pg, 12 pg, 25 pg, 50 pg, 75 pg and 150 pg per embryo. Use of 12 pg per embryo was optimal for epiboly rescue when injected at the 1-cell stage. As controls for mRNA, we injected unrelated H2B mRNA and dextran in YSL of wild-type and mutant embryos, also at the 512-cell stage. miR-430 or mismatch microRNAs were injected in the range 1.25 to 10 nM per embryo; 10 nM miR-430 per embryo resulted in the best epiboly rescue.

Visualization of YSL, YSL nuclei and time-lapse recording of live embryos

To visualize yolk syncytial nuclei (YSN), we injected 1 nl of 0.25 mM of SYTOX Green (Thermo Fisher Scientific) mixed with 0.2 M KCl into wild-type and MZ*nanog* embryos at the 512-cell stage as described by D'Amico and Cooper (2001). Several embryos were embedded into 1.5% low melting

Development (2018) 145, dev155366. doi:10.1242/dev.155366

agarose and simultaneously recorded for up to 5 h with a Leica MZ16 FA stereo-fluorescence microscope and a Leica DFC 350 FX camera. Additionally, wild-type and MZ*nanog* embryos were injected with SYTOX Green and tetramethylrhodamine dextran (12.5 ng per embryo), embedded in 1% low melting agarose, placed in a Zeiss capillary and imaged with ZEISS Lightsheet Z.1 equipped with W Plan-Apochromat 10×/0.5NA (water immersion) Working Distance=3.7 mm and W Plan-Apochromat 20×/1.0NA Corr (water immersion) Working Distance=2.4 mm objectives at 4.7 hpf. Four-version *z*-stack pictures were processed with Zeiss ZEN black 2014 (dual side fusion and multi-view processing). Lightsheet *z*-stack overview pictures of the lateral halves of the embryos were exported via Arivis Vision4D. Green channel was subtracted from the red channel in the Lightsheet images to increase the visibility of the YSL nuclei (green) within the YSL cytoplasm (red).

Visualization of cell membranes and nuclei in fixed embryos

To visualize the cell membranes and cell nuclei, embryos were fixed at 3 hpf with 4% PFA overnight at 4°C. Then the embryos were washed in PBST and dechorionated. For permeabilization, the embryos were treated either with a combination of 0.5% Triton X-100 and 0.5% NP40 for 1 h or in a PBSDT solution (1% DMSO and 0.3% Triton X-100 in PBST) overnight. In order to stain the deep cells as well, the embryos were washed thrice in 0.3% Triton X-100 in PBST and afterwards stained in PBSDT. Wild-type and MZ*nanog* embryos were stained with a rhodamine-phalloidin staining solution (6.6 µM; 1:100 in PBSDT) for 2 days. While the embryos were in the staining solution, they were first kept at RT for 4 h and then on a slow shaker at 4°C. The embryos were always kept in the dark. They were washed with PBST to stop the staining and a SYTOX Green staining solution (5 mM; 1:40,000 in PBSDT) was added afterwards. The embryos were stained in the dark for 1 h and 10 min at RT. To stop the staining, the embryos were washed once in PBSDT for 15 min and then once with PBST for 15 min. They were then embedded in 1.5% low-melting agarose and images were taken with a Zeiss LSM 510 META NLO confocal inverted microscope.

Cell division counting in living embryos

SYTOX Green (0.2 mM, Thermo Fisher Scientific) was mixed with 0.2 M KCl and 1 nl was injected into wild-type and *MZnanog* mutant embryos at the 1-cell stage. Embryos that showed sufficient SYTOX Green fluorescence were selected under the fluorescence stereomicroscope and placed in a furrow of an agarose plate. They were covered with a 24×60 mm cover slide, which was fixed with 2% low melting agarose and overlaid with 0.3× Danieau's buffer to prevent drying out of the embryos. Subsequently, the development of the embryos was documented using a Leica MZ16 FA fluorescence stereomicroscope and Leica Microsystems LAS AF software, which took a brightfield image and a fluorescent image (GFP filter, 395 nm) every 3 min until the next morning. The temperature during documentation was 25°C. Resulting images were analyzed with ImageJ by counting the single images between each cell division. The obtained number of images was multiplied by 3 min to achieve the time span in minutes between the cell divisions.

Estimating of mitotic frequency in fixed embryos

We used a modified procedure from Kotkamp et al. (2014). Embryos were fixed at 3, 4 and 4.7 hpf in Gard's FG fixative for 2 h and incubated overnight in PBST containing 0.33 M glycine. After manual dechrorionation, embryos were stored in methanol in −20°C. Then 30-50 embryos per stage per genotype were washed five times in PBSTX (1× PBST, 0.3% Triton X-100), stained with SYTOX Green working solution (5 mM; 1:40,000 in PBSTX) for 30 min, washed three times in PBST and transferred into 90% glycerol in PBS. One image per embryo was taken at animal-lateral view with a Leica MZ16 FA stereo-fluorescence microscope and a Leica DFC 350 FX camera (75×, 300 ms, 3.0 gain) in the GFP channel. Images were processed with Adobe Photoshop CS6 ('Unsharp Mask' filter, amount: 150%, radius: 5 pixels, threshold: 0), then brightness and contrast were automatically adjusted in ImageJ (open source software). Total nuclei and mitotic nuclei were counted manually (Fig. S1C,D). 'Mitotic cells' refer to the cells going through metaphase and anaphase, for which the elongated shape of chromosomes could be easily recognized (Fig. S1D, arrows). Metaphase plates were counted as one, and anaphase as two mitotic cells. The ratio of mitotic to total cells was expressed in mitoses per 100 cells.

Staining and semi-automatic counting of the dead cells

For detection of dead (apoptotic) cells we used a modified Acridine Orange staining procedure (Westerfield, 2000). At 9 hpf (when the non-injected wild-type control embryos reached 90% epiboly), living embryos were transferred to 5 µg/ml Acridine Orange (AO) solution in egg water and incubated for 30 min. The embryos were washed in the egg water three times for 15 min on a slowly rotating shaker in the dark. Images (15-30 per condition) were taken in GFP channel using a Leica MZ16FA microscope equipped with a Leica DFC350FX camera. Acquisition of images lasted several hours until wild-type controls reached the 3- to 6-somite stage, therefore care was taken to alternate control and experimental images. Exposure time was kept the same for all the images; no bleaching was observed. Images were then semi-automatically processed to quantify dead cells as illustrated in Fig. S2. Images in TIFF format were batch-processed in Adobe Photoshop ('Unsharp Mask' filter, amount: 244, radius: 9.3 pixels, threshold: 0). Total area, number and average size of AO-stained spots was recorded for each image as shown in Fig. S2 in ImageJ using the macro:

```
//run("Threshold…");
setThreshold(60, 255);
run("Analyze Particles…", "size=4-100 show=Nothing display exclude
summarize");
run("Open Next").
```

The macro was run with three different thresholds for each experiment. Statistical differences in cell death (expressed as either total area or number of AO-stained spots per embryo, Fig. S2) between the experimental groups were threshold-independent. The results were expressed as total area of AO-stained spots and normalized to mean MZ*nanog* control value.

Visualization of actin structures in fixed embryos

Embryos were fixed at the desired stage in 4% PFA overnight at 4°C. After washing thrice in PBST, rhodamine phalloidin (1:500 in PBST) was added and incubated at RT for 4 h in the dark. Embryos were washed twice in PBST for 15 min to remove unbound rhodamine phalloidin. Subsequently, the embryos were mounted on a slide with a hollow in a drop of Dako Faramount Aqueous Mounting Medium and covered with a cover slide. Embryos were documented using a Zeiss Axio Examiner D1 microscope, an AxioCam MRc camera and Zen 2012 blue edition software (Zeiss), using the Alexa 555 emission filter. Images were edited with Zen 2012 SP1 black edition software.

Visualization of microtubules in fixed embryos

For visualization of the microtubules, embryos were fixed in Gard's FG fixative and anti-β-Tubulin staining (clone KMX-1 at 1:500, Merck, MAB3408) was performed as previously described (Gard, 1991; Solnica-Krezel and Driever, 1994).

Quantitative RT-PCR

Quantitative RT-PCR was performed as described by Onichtchouk et al. (2010). *rpl5b* was used as a normalization control. Sequences of PCR primers are listed in Table S4.

Generation of *her3*-GFP transgenic line

To obtain a *her3enh1-GFP* reporter construct, we inserted EGFP downstream of the 2.2 kb *her3* regulatory sequence in the PCRII-topo vector (Onichtchouk et al., 2010). The region containing *her3GFP* sequence was excised, gel-purified and microinjected into F0 AB-TL fish to achieve random integration into the genome. The F1 fish positive for integration were selected at 24 hpf by EGFP fluorescence pattern, recapitulating *her3* expression (Hans et al., 2004), and further crossed. The Tg(*her3enh1-GFP*) was recorded in the internal database under allele number m1430 and is available upon request.

Cell transplantations

Transplantations were performed as described by Ho and Kimmel (Ho and Kimmel, 1993). The wild-type and MZ*nanog* donor cells were labeled with dextran Alexa Fluor 488 and tetramethylrhodamine dextran, MW 10 KDa (Thermo Fisher Scientific, 12.5 ng per embryo) by injecting into the 1-cell stage. Five to 15 cells were taken from the injected wild-type donor and

MZ*nanog* donor at sphere stage (4 hpf) and simultaneously transplanted into the wild-type recipient at the sphere stage, using the same transplantation needle. Pictures were taken from 24 hpf embryos using a Zeiss Axio Examiner D1 microscope and a Zeiss AxioCam MRc camera. The order of transplantations and labeling colors between wild-type and MZ*nanog* donors was swapped in each experiment (ten experiments in total, Table S1). Transplanted cells were scored in 52 embryos in total. Embryos were selected for scoring using the following criteria: at least one recognizable cell type labeled with the first color and any (including unknown) cells labeled with the second color should be visible in the same embryo. Cell numbers and genotypes of transplanted cells in each of 52 embryos analyzed are listed in Table S3.

Acknowledgements
We thank Wolfgang Driever and Sebastian Arnold for discussion, and Anna Gebhard, Rainer Duden, Lev Yampolsky, Logan Doil and anonymous reviewers for comments on earlier versions of the manuscript. We are grateful to James Gagnon and Alex Schier for sharing their data before publication. We are also grateful to Sabine Goetter for excellent fish care and to Andrea Buderer for administrative support, and to LIC for the demonstration of Lightsheet Microscopy.

Competing interests
The authors declare no competing or financial interests.

Author contributions
Conceptualization: M.V., D.O.; Methodology: M.V.; Formal analysis: V.K.; Investigation: M.V., M.A.S., M.G., V.K., L.B.; Resources: M.V., M.A.S., M.G.; Writing - original draft: M.V.; Writing - review & editing: M.V., D.O.; Visualization: M.V., M.A.S., M.G., L.B., R.G.; Supervision: D.O.; Project administration: D.O.; Funding acquisition: D.O.

Funding
This work was supported by Deutsche Forschungsgemeinschaft (DFG-ON86/4-1 and DFG-EXC294 A7-2 to D.O.).

Supplementary information
Supplementary information available online at
http://dev.biologists.org/lookup/doi/10.1242/dev.155366.supplemental

References
Alexander, J. and Stainier, D. Y. R. (1999). A molecular pathway leading to endoderm formation in zebrafish. *Curr. Biol.* **9**, 1147-1157.
Alexander, J., Rothenberg, M., Henry, G. L. and Stainier, D. Y. R. (1999). casanova plays an early and essential role in endoderm formation in zebrafish. *Dev. Biol.* **215**, 343-357.
Bae, Y.-K., Shimizu, T. and Hibi, M. (2005). Patterning of proneuronal and inter-proneuronal domains by hairy- and enhancer of split-related genes in zebrafish neuroectoderm. *Development* **132**, 1375-1385.
Belting, H. G., Wendik, B., Lunde, K., Leichsenring, M., Mossner, R., Driever, W. and Onichtchouk, D. (2011). Pou5f1 contributes to dorsoventral patterning by positive regulation of vox and modulation of fgf8a expression. *Dev. Biol.* **356**, 323-336.
Boyer, L. A., Lee, T. I., Cole, M. F., Johnstone, S. E., Levine, S. S., Zucker, J. P., Guenther, M. G., Kumar, R. M., Murray, H. L., Jenner, R. G. et al. (2005). Core transcriptional regulatory circuitry in human embryonic stem cells. *Cell* **122**, 947-956.
Bruce, A. E. E. (2016). Zebrafish epiboly: spreading thin over the yolk. *Dev. Dyn.* **245**, 244-258.
Bruce, A. E. E., Howley, C., Dixon Fox, M. and Ho, R. K. (2005). T-box gene eomesodermin and the homeobox-containing Mix/Bix gene mtx2 regulate epiboly movements in the zebrafish. *Dev. Dyn.* **233**: 105-114.
Carlson, D. F., Tan, W., Lillico, S. G., Stverakova, D., Proudfoot, C., Christian, M., Voytas, D. F., Long, C. R., Whitelaw, C. B. A. and Fahrenkrug, S. C. (2012). Efficient TALEN-mediated gene knockout in livestock. *Proc. Natl. Acad. Sci. USA* **109**, 17382-17387.
Cermak, T., Doyle, E. L., Christian, M., Wang, L., Zhang, Y., Schmidt, C., Baller, J. A., Somia, N. V., Bogdanove, A. J. and Voytas, D. F. (2011). Efficient design and assembly of custom TALEN and other TAL effector-based constructs for DNA targeting. *Nucleic Acids Res.* **39**, e82.
Chambers, I., Silva, J., Colby, D., Nichols, J., Nijmeijer, B., Robertson, M., Vrana, J., Jones, K., Grotewold, L. and Smith, A. (2007). Nanog safeguards pluripotency and mediates germline development. *Nature* **450**, 1230-1234.
Chen, S. and Kimelman, D. (2000). The role of the yolk syncytial layer in germ layer patterning in zebrafish. *Development* **127**, 4681-4689.
Cheng, J. C., Miller, A. L. and Webb, S. E. (2004). Organization and function of microfilaments during late epiboly in zebrafish embryos. *Dev. Dyn.* **231**, 313-323.
D'Amico, L. A. and Cooper, M. S. (2001). Morphogenetic domains in the yolk syncytial layer of axiating zebrafish embryos. *Dev. Dyn.* **222**, 611-624.
David, N. B. and Rosa, F. M. (2001). Cell autonomous commitment to an endodermal fate and behaviour by activation of Nodal signalling. *Development* **128**, 3937-3947.
Dee, C. T., Gibson, A., Rengifo, A., Sun, S.-K., Patient, R. K. and Scotting, P. J. (2007). A change in response to Bmp signalling precedes ectodermal fate choice. *Int. J. Dev. Biol.* **51**, 79-84.
Dougan, S. T., Warga, R. M., Kane, D. A., Schier, A. F. and Talbot, W. S. (2003). The role of the zebrafish nodal-related genes squint and cyclops in patterning of mesendoderm. *Development* **130**, 1837-1851.
Du, S., Draper, B. W., Mione, M., Moens, C. B. and Bruce, A. (2012). Differential regulation of epiboly initiation and progression by zebrafish Eomesodermin A. *Dev. Biol.* **362**, 11-23.
Frum, T., Halbisen, M. A., Wang, C., Amiri, H., Robson, P. and Ralston, A. (2013). Oct4 cell-autonomously promotes primitive endoderm development in the mouse blastocyst. *Dev. Cell* **25**, 610-622.
Gagnon, J. A., Obbad, K. and Schier, A. F. (2018). The primary role of zebrafish *nanog* is in extra-embryonic tissue. *Development* **145**, dev147793.
Gard, D. L. (1991). Organization, nucleation, and acetylation of microtubules in Xenopus laevis oocytes: a study by confocal immunofluorescence microscopy. *Dev. Biol.* **143**, 346-362.
Giraldez, A. J., Cinalli, R. M., Glasner, M. E., Enright, A. J., Thomson, J. M., Baskerville, S., Hammond, S. M., Bartel, D. P. and Schier, A. F. (2005). MicroRNAs regulate brain morphogenesis in zebrafish. *Science* **308**, 833-838.
Giraldez, A. J., Mishima, Y., Rihel, J., Grocock, R. J., Van Dongen, S., Inoue, K., Enright, A. J. and Schier, A. F. (2006). Zebrafish MiR-430 promotes deadenylation and clearance of maternal mRNAs. *Science* **312**, 75-79.
Hans, S., Scheer, N., Riedl, I., v Weizsacker, E., Blader, P. and Campos-Ortega, J. A. (2004). her3, a zebrafish member of the hairy-E(spl) family, is repressed by Notch signalling. *Development* **131**, 2957-2969.
Henry, G. L. and Melton, D. A. (1998). Mixer. a homeobox gene required for endoderm development. *Science* **281**, 91-96.
Hirata, T., Yamanaka, Y., Ryu, S.-L., Shimizu, T., Yabe, T., Hibi, M. and Hirano, T. (2000). Novel mix-family homeobox genes in zebrafish and their differential regulation. *Biochem. Biophys. Res. Commun.* **271**, 603-609.
Ho, R. K. and Kimmel, C. B. (1993). Commitment of cell fate in the early zebrafish embryo. *Science* **261**, 109-111.
Holzschuh, J., Barrallo-Gimeno, A., Ettl, A. K., Durr, K., Knapik, E. W. and Driever, W. (2003). Noradrenergic neurons in the zebrafish hindbrain are induced by retinoic acid and require tfap2a for expression of the neurotransmitter phenotype. *Development* **130**, 5741-5754.
Hong, S.-K., Jang, M. K., Brown, J. L., McBride, A. A. and Feldman, B. (2011). Embryonic mesoderm and endoderm induction requires the actions of non-embryonic Nodal-related ligands and Mxtx2. *Development* **138**, 787-795.
Iwafuchi-Doi, M., Yoshida, Y., Onichtchouk, D., Leichsenring, M., Driever, W., Takemoto, T., Uchikawa, M., Kamachi, Y. and Kondoh, H. (2011). The Pou5f1/Pou3f-dependent but SoxB-independent regulation of conserved enhancer N2 initiates Sox2 expression during epiblast to neural plate stages in vertebrates. *Dev. Biol.* **352**, 354-366.
Kane, D. A., Warga, R. M. and Kimmel, C. B. (1992). Mitotic domains in the early embryo of the zebrafish. *Nature* **360**, 735-737.
Kimmel, C. B. and Law, R. D. (1985). Cell lineage of zebrafish blastomeres. II. Formation of the yolk syncytial layer. *Dev. Biol.* **108**, 86-93.
Kimmel, C. B., Ballard, W. W., Kimmel, S. R., Ullmann, B. and Schilling, T. F. (1995). Stages of embryonic development of the zebrafish. *Dev. Dyn.* **203**, 253-310.
Kok, F. O., Shin, M., Ni, C. W., Gupta, A., Grosse, A. S., van Impel, A., Kirchmaier, B. C., Peterson-Maduro, J., Kourkoulis, G., Male, I. et al. (2015). Reverse genetic screening reveals poor correlation between morpholino-induced and mutant phenotypes in zebrafish. *Dev. Cell* **32**, 97-108.
Koppen, M., Fernandez, B. G., Carvalho, L., Jacinto, A. and Heisenberg, C. P. (2006). Coordinated cell-shape changes control epithelial movement in zebrafish and Drosophila. *Development* **133**, 2671-2681.
Kotkamp, K., Kur, E., Wendik, B., Polok, B. K., Ben-Dor, S., Onichtchouk, D. and Driever, W. (2014). Pou5f1/Oct4 promotes cell survival via direct activation of mych expression during zebrafish gastrulation. *PLoS ONE* **9**, e92356.
Lachnit, M., Kur, E. and Driever, W. (2008). Alterations of the cytoskeleton in all three embryonic lineages contribute to the epiboly defect of Pou5f1/Oct4 deficient MZspg zebrafish embryos. *Dev. Biol.* **315**, 1-17.
Le Bin, G. C., Munoz-Descalzo, S., Kurowski, A., Leitch, H., Lou, X., Mansfield, W., Etienne-Dumeau, C., Grabole, N., Mulas, C., Niwa, H. et al. (2014). Oct4 is required for lineage priming in the developing inner cell mass of the mouse blastocyst. *Development* **141**, 1001-1010.
Lee, M. T., Bonneau, A. R., Takacs, C. M., Bazzini, A. A., Divito, K. R., Fleming, E. S. and Giraldez, A. J. (2013). Nanog, Pou5f1 and SoxB1 activate zygotic gene expression during the maternal-to-zygotic transition. *Nature* **503**, 360-364.

Leichsenring, M., Maes, J., Mossner, R., Driever, W. and Onichtchouk, D. (2013). Pou5f1 transcription factor controls zygotic gene activation in vertebrates. *Science* **341**, 1005-1009.
Loh, K. M. and Lim, B. (2011). A precarious balance: pluripotency factors as lineage specifiers. *Cell Stem Cell* **8**, 363-369.
Loh, Y. H., Wu, Q., Chew, J. L., Vega, V. B., Zhang, W., Chen, X., Bourque, G., George, J., Leong, B., Liu, J. et al. (2006). The Oct4 and Nanog transcription network regulates pluripotency in mouse embryonic stem cells. *Nature Genetics* **38**, 431-440.
Lunde, K., Belting, H. G. and Driever, W. (2004). Zebrafish pou5f1/pou2. homolog of mammalian Oct4, functions in the endoderm specification cascade. *Curr. Biol.* **14**, 48-55.
Mitsui, K., Tokuzawa, Y., Itoh, H., Segawa, K., Murakami, M., Takahashi, K., Maruyama, M., Maeda, M. and Yamanaka, S. (2003). The homeoprotein Nanog is required for maintenance of pluripotency in mouse epiblast and ES cells. *Cell* **113**, 631-642.
Morita, H., Grigolon, S., Bock, M., Krens, S. F. G., Salbreux, G. and Heisenberg, C.-P. (2017). The physical basis of coordinated tissue spreading in zebrafish gastrulation. *Dev. Cell* **40**, 354-366.e4.
Neff, K. L., Argue, D. P., Ma, A. C., Lee, H. B., Clark, K. J. and Ekker, S. C. (2013). Mojo hand, a TALEN design tool for genome editing applications. *BMC Bioinformatics* **14**, 1.
Okuda, Y., Ogura, E., Kondoh, H. and Kamachi, Y. (2010). B1 SOX coordinate cell specification with patterning and morphogenesis in the early zebrafish embryo. *PLoS Genet.* **6**, e1000936.
Onichtchouk, D. and Driever, W. (2016). Zygotic genome activators, developmental timing, and pluripotency. *Curr. Top. Dev. Biol.* **116**, 273-297.
Onichtchouk, D., Geier, F., Polok, B., Messerschmidt, D. M., Mossner, R., Wendik, B., Song, S., Taylor, V., Timmer, J. and Driever, W. (2010). Zebrafish Pou5f1-dependent transcriptional networks in temporal control of early development. *Mol. Syst. Biol.* **6**, 354.
Perez-Camps, M., Tian, J., Chng, S. C., Sem, K. P., Sudhaharan, T., Teh, C., Wachsmuth, M., Korzh, V., Ahmed, S. and Reversade, B. (2016). Quantitative imaging reveals real-time Pou5f3-Nanog complexes driving dorsoventral mesendoderm patterning in zebrafish. *Elife* **5**, e11475.
Radzisheuskaya, A., Chia Gle, B., dos Santos, R. L., Theunissen, T. W., Castro, L. F. C., Nichols, J. and Silva, J. C. R. (2013). A defined Oct4 level governs cell state transitions of pluripotency entry and differentiation into all embryonic lineages, *Nat. Cell Biol.* **15**, 579-590.
Reim, G. and Brand, M. (2006). Maternal control of vertebrate dorsoventral axis formation and epiboly by the POU domain protein Spg/Pou2/Oct4. *Development* **133**, 2757-2770.
Reim, G., Mizoguchi, T., Stainier, D. Y., Kikuchi, Y. and Brand, M. (2004). The POU domain protein spg (pou2/Oct4) is essential for endoderm formation in cooperation with the HMG domain protein casanova. *Dev. Cell* **6**, 91-101.
Reiter, J. F., Alexander, J., Rodaway, A., Yelon, D., Patient, R., Holder, N. and Stainier, D. Y. R. (1999). Gata5 is required for the development of the heart and endoderm in zebrafish. *Genes Dev.* **13**, 2983-2995.
Schuff, M., Siegel, D., Philipp, M., Bundschu, K., Heymann, N., Donow, C. and Knochel, W. (2011). Characterization of Danio rerio nanog and functional comparison to xenopus vents. *Stem Cells Dev.* **3**, 3.
Schulte-Merker, S., van Eeden, F. J., Halpern, M. E., Kimmel, C. B. and Nüsslein-Volhard, C. (1994). no tail (ntl) is the zebrafish homologue of the mouse T (Brachyury) gene. *Development* **120**, 1009-1015.
Silva, J., Nichols, J., Theunissen, T. W., Guo, G., van Oosten, A. L., Barrandon, O., Wray, J., Yamanaka, S., Chambers, I. and Smith, A. (2009). Nanog is the gateway to the pluripotent ground state. *Cell* **138**, 722-737.
Solnica-Krezel, L. (2006). Gastrulation in zebrafish – all just about adhesion? *Curr. Opin. Genet. Dev.* **16**, 433-441.
Solnica-Krezel, L. and Driever, W. (1994). Microtubule arrays of the zebrafish yolk cell: organization and function during epiboly. *Development* **120**, 2443-2455.
Song, S., Eckerle, S., Onichtchouk, D., Marrs, J. A., Nitschke, R. and Driever, W. (2013). Pou5f1-dependent EGF expression controls E-cadherin endocytosis, cell adhesion, and zebrafish epiboly movements. *Dev. Cell* **24**, 486-501.
Takahashi, K. and Yamanaka, S. (2006). Induction of pluripotent stem cells from mouse embryonic and adult fibroblast cultures by defined factors. *Cell* **126**, 663-676.
Teo, A. K. K., Arnold, S. J., Trotter, M. W. B., Brown, S., Ang, L. T., Chng, Z., Robertson, E. J., Dunn, N. R. and Vallier, L. (2011). Pluripotency factors regulate definitive endoderm specification through eomesodermin. *Genes Dev.* **25**, 238-250.
Theunissen, T. W., Costa, Y., Radzisheuskaya, A., van Oosten, A. L., Lavial, F., Pain, B., Castro, L. F. C. and Silva, J. C. R. (2011). Reprogramming capacity of Nanog is functionally conserved in vertebrates and resides in a unique homeodomain. *Development* **138**, 4853-4865.
Thomson, M., Liu, S. J., Zou, L.-N., Smith, Z., Meissner, A. and Ramanathan, S. (2011). Pluripotency factors in embryonic stem cells regulate differentiation into germ layers. *Cell* **145**, 875-889.
Wang, H., Liu, Y., Ye, D., Li, J., Liu, J. and Deng, F. (2016). Knockdown of zebrafish Nanog increases primordial germ cells during early embryonic development. *Dev. Growth Differ.* **58**, 355-366.
Warga, R. M. and Kimmel, C. B. (1990). Cell movements during epiboly and gastrulation in zebrafish. *Development* **108**, 569-580.
Warga, R. M. and Nüsslein-Volhard, C. (1999). Origin and development of the zebrafish endoderm. *Development* **126**, 827-838.
Westerfield, M. (2000). *The Zebrafish Book: A Guide to the Laboratory Use of Zebrafish (Danio rerio)*. Eugene, OR: Univ. of Oregon Press.
Wilkins, S. J., Yoong, S., Verkade, H., Mizoguchi, T., Plowman, S. J., Hancock, J. F., Kikuchi, Y., Heath, J. K. and Perkins, A. C. (2008). Mtx2 directs zebrafish morphogenetic movements during epiboly by regulating microfilament formation. *Dev. Biol.* **314**, 12-22.
Xu, C., Fan, Z. P., Muller, P., Fogley, R., Dibiase, A., Trompouki, E., Unternaehrer, J., Xiong, F., Torregroza, I., Evans, T. et al. (2012). Nanog-like regulates endoderm formation through the Mxtx2-Nodal pathway. *Dev. Cell* **22**, 625-638.
Zalik, S. E., Lewandowski, E., Kam, Z. and Geiger, B. (1999). Cell adhesion and the actin cytoskeleton of the enveloping layer in the zebrafish embryo during epiboly. *Biochem. Cell Biol.* **77**, 527-542.